



PONTIFICIA UNIVERSIDAD CATOLICA DE CHILE
ESCUELA DE INGENIERIA

**EROSION UNDER TURBULENT SLURRY
FLOW: AN EXPERIMENTAL
DETERMINATION OF PARTICLE
IMPACT CONDITIONS AND
DISTRIBUTION THEREOF BY IMAGE
PROCESSING**

NICOLÁS ANDRÉS MOLINA VERGARA

Thesis submitted to the Office of Research and Graduate Studies in partial fulfillment of the requirements for the Degree of Master of Science in Engineering.

Advisor:

MAGDALENA WALCZAK

Santiago de Chile, July, 2020

© 2020, Nicolás Andrés Molina Vergara



PONTIFICIA UNIVERSIDAD CATOLICA DE CHILE
ESCUELA DE INGENIERIA

**EROSION UNDER TURBULENT SLURRY
FLOW: AN EXPERIMENTAL DETERMINATION
OF PARTICLE IMPACT CONDITIONS AND
DISTRIBUTION THEREOF BY IMAGE
PROCESSING**

NICOLÁS ANDRÉS MOLINA VERGARA

Members of the Committee:

MAGDALENA WALCZAK

DIEGO CELENTANO

REMIGIUSZ MICHALCZEWSKI

LUIS RIZZI

Thesis submitted to the Office of Research and Graduate Studies in partial fulfillment of the requirements for the Degree of Master of Science in Engineering.

Santiago de Chile, July, 2020

To my family *Molina Vergara*, for their unconditional love and support.

Trust in the Lord with all thine heart; and lean not unto thine own understanding. In all thy ways acknowledge him, and he shall direct thy paths. (Proverbs 3:5-6, KJV)

ACKNOWLEDGEMENTS

First and foremost, to the one who brought from death to life: the Father, the Son (Jesus Christ), and the Holy Spirit.

While studying in my first semester of BSE at Pontificia Universidad Católica de Chile, I immediately looked for the opportunity to do scientific research at the School of Engineering. Surprisingly, I got a research assistant work in my first university holidays in the Department of Mechanical and Metallurgical Engineering with the professor Magdalena Walczak, who would become several years later my supervisor in the master's degree. I am deeply grateful for her great support throughout these years. She is one of the smartest people I have ever met both academically and philosophically.

On the other hand, the unconditional love of my family has been a hallmark that has helped me achieve many dreams in my life, including this thesis. My mother, M. Angélica Vergara, for her care and moral support. My father, Jaime Molina, for his words of wisdom and encouragement to take risks. My sister, Valentina Molina, for her emotional sharpness and happiness that shines more than anything else.

Finally, I would like to convey special thanks to people who helped to conduct and discussing this work: Remigiusz Michalczewski, Marek Kalbarczyk and Dr. Edyta Osuch-Słomka from Łukasiewicz Research Network - Institute for Sustainable Technologies (Radom, Poland), and Dr. Javiera Aguirre, Patricio Pérez and Matías Cristi from the Department of Mechanical and Metallurgical Engineering, Escuela de Ingeniería, Pontificia Universidad Católica de Chile (Santiago, Chile).

This research has been funded by CONICYT through grants REDES170071, FONDEQUIP EQM160091 and scholarship CONICYT-PCHA/Magister Nacional/2019-22191158.

TABLE OF CONTENTS

DEDICATION	ii
ACKNOWLEDGEMENTS	iii
LIST OF TABLES	vii
LIST OF FIGURES.....	viii
NOMENCLATURE.....	xi
RESUMEN.....	xii
ABSTRACT	xiii
LIST OF PAPERS.....	xiv
1. INTRODUCTION	1
2. LITERATURE REVIEW	4
2.1. Slurry erosion	4
2.1.1. Fundamentals of erosion mechanisms	4
2.1.2. Fundamentals of erosion mechanisms	7
2.2. Erosion modelling	12
2.2.1. Oka model.....	12
2.2.2. Huang model.....	13
2.2.3. Cheng model.....	13
2.3. Image processing.....	14
3. THESIS PROPOSAL	17
3.1 Hypothesis.....	17
3.2 General objective.....	17
3.3 Specific objectives.....	17

4.	EXPERIMENTAL.....	19
4.1	Sample preparation.....	19
4.2	Erodent preparation.....	20
4.3	Experimental rig.....	22
4.4	Experimental procedure.....	23
4.5	Surface analysis method.....	25
4.5.1	Digital image acquisition.....	25
4.5.2	Digital image processing.....	25
4.5.3	Digital image analysis.....	27
4.6	Global coordinates and kinetic energy.....	29
4.7	Erosion models.....	31
4.7.1	Oka model.....	31
4.7.2	Huang model.....	32
4.7.3	Cheng model.....	32
4.7.4	Solving method procedure.....	32
5.	RESULTS.....	33
5.1	Individual and collective features.....	33
5.2	Local coordinates – Impact direction.....	34
5.3	Local coordinates – Impact angle.....	35
5.4	Global coordinates – Inclination and azimuth angle.....	36
5.5	Normalized kinetic energy.....	38
5.6	Wear rate by weight loss.....	39
5.7	Impact conditions for modelling.....	40
5.8	Impact velocity.....	41
5.9	Wear correlation.....	43
6.	DISCUSSION.....	44
6.1	Impact flow conditions.....	44
6.2	Particle impact conditions.....	48
6.3	Implications for wear analysis.....	50
6.4	Feasibility of the diagnostic tool.....	51

6.5	Dimensions of individual erosion wear scars.....	54
6.6	Erosion models.....	55
6.7	Wear correlation: Feasibility of the inverse analysis	57
7.	CONCLUSIONS	60
	References	62
	Appendix.....	75
	Appendix A: Sample machining.....	76
	Appendix B: Particle morphology.....	77
	Appendix C: Corrosion by-products	78

LIST OF TABLES

Table 1. Properties of frequently used erodent particles (Javaheri et al., 2018).	10
Table 2. Particle shape and size descriptors relevant for wear (Raadnui, 2005).....	16
Table 3. Physical and mechanical properties of Cu-ETP used in this study.	19
Table 4. Details of the processes used for surface finish prior exposure.	20
Table 5. Physical and mechanical properties of the glass beads.	20
Table 6. Particle size ranges used in this study.	21
Table 7. Slurry concentration for different particle sizes.....	23
Table 8. Theoretical kinetic energy of erodent flow and generalized Stokes number evaluated for nominal linear speed of 10 m/s.....	24
Table 9. Statistical tests for verifying the hypothesis of Gaussian distribution. Values determined by Kolmogorov-Smirnov (KS) and Anderson-Darling (AD) tests.	46
Table 10. Spearman's rank correlation coefficient between impact direction and impact angle at different particle sizes.	49
Table 11. Machining parameters for Cu-ETP recommended by ASM/DKI.....	76

LIST OF FIGURES

Figure 1. Schematic illustration of a) ploughing and b) cutting erosion mechanism. Adapted from (Javaheri et al., 2018).	5
Figure 2. Schematic representation of erosion caused by deformation mechanism at normal impact and cutting mechanism at oblique impact in a) ductile and b) brittle materials (Y. F. Wang & Yang, 2008).	5
Figure 3. Fishbone of important parameters influencing slurry erosion (Javaheri et al., 2018)	7
Figure 4. Volume loss and average near-surface hardness data for steel plate and steel pipe materials (H. M. Clark & Llewellyn, 2001).	9
Figure 5. SEM images of a) alumina, b) silicon carbide, c) quartz, d) glass beads, e) steel round grit, f) tungsten carbide, g) diamond, and cross-section SEM images of h) chromite, i) concentrate, j) matte, k) ore, and l) tailings. Retrieved from Javaheri et al. (2018).	10
Figure 6. Variation of erosion rate with impact angle for brittle and ductile materials (Nandre & Desale, 2018).	11
Figure 7. Image analysis for SEM micrographs obtained for different flow velocities: FFT – fast Fourier transform, FFT-ZT – contrast adjusted visualization of selected FFT zone (red rectangle), HIST – histogram of wear scar orientation (δ) as determined by image analysis of FFT-ZT (Molina et al., 2019)	15
Figure 8. A representative shape of glass beads (50-60 mesh, d_p of 276 μm) observed under SEM. For other mesh sizes see Figure 28 in Appendix B.	21
Figure 9. Overview of the experimental set-up. For better visibility of the test samples, the pot is filled with water instead of slurry.	22
Figure 10. Schematic sequence of the image processing procedure to select data of individual scars from the collective profilometry data.	26
Figure 11. Geometrical description of global coordinates of inclination (θ) and azimuth (φ) angles, and the local coordinates of the direction of impact (δ) and impact angle (α).	27
Figure 12. Example of experimental determination of impact angle (α) along the impact direction (δ) for a single particle impact.	28

Figure 13. 3D profilometry example of a wear scar produced after erosive exposure.	29
Figure 14. Representative SEM micrographs of: a) individual and b) collective features of wear scars produced by particles of d_p of 276 μm	33
Figure 15. Summary of impact direction distribution determined for each particle size....	34
Figure 16. Summary of impact angle distributions determined for each particle size.....	36
Figure 17. Summary of a) inclination angle (θ) and b) azimuth angle (φ) distributions determined for each particle size.....	37
Figure 18. Summary of the normalized normal component of kinetic energy distribution determined for each particle size.....	38
Figure 19. Wear rate determined by weight loss in function of particle size. The dash-dotted line is a visual guide only to connect the triangle markers. The error bars in the particle size correspond to the mesh size. Error bars in the wear rate correspond to experimental statistics.	39
Figure 20. Summary of distributions for different particle sizes: (a) impact angle, (b) indentation depth, and (c) wear volume. Red line connects the median of each distribution.	40
Figure 21. Summary of impact velocity and kinetic energy distribution for different particle sizes: Oka (a,b), Huang (c,d), and Cheng (e,f) erosion models. Red line connects the median of each distribution.....	42
Figure 22. Heatmap of the Spearman correlation matrix for experimental variables.	43
Figure 23. Example of a) Gaussian probability quantile-quantile plot (blue: data, red: Gaussian slope) and b) Point histogram plot (blue: data – bin size of 5° ; red: Gaussian fit) for 548 μm d_p	46
Figure 24. Example of correlation between impact direction and impact angle determined for the particle size of 276 μm	50
Figure 25. Wear scar detection of scar pattern produced by the particle size of 774 μm . White boxes enclose the identified wear scars. Detected features are shown in a matrix of four combinations of threshold parameters: SDFG ($\sigma = 3$ or 2) and TMWSS (9×9 or 5×5).	53
Figure 26. Wear damage normalized by erodent mass: (a) Indentation depth, (b) Wear volume.....	55

Figure 27. Scatter plot of wear volume per: a) erodent mass and b) impact kinetic energy of erodent (estimated from Cheng model, Fig. 6). Linear regression only was shown to visually guide the correlation between the variables. 58

Figure 28. Representative SEM appearance of the erodent. Glass beads sieved by the mesh sizes: a) 20-25, b) 25-30, c) 30-35, d) 34-40, and e) 50-60..... 77

Figure 29. Example of SEM surface conditions after 1 h of exposure in distilled water. Nominal speed at the shaft surface 10 m/s. General appearance at magnification $\times 400$ (a) and example of local appearance at magnification $\times 4,000$ (b). 78

NOMENCLATURE

Symbol Description Units

E_k : kinetic energy (M L² T⁻²)

V : impact velocity (L T⁻¹)

d_p : particle size (L)

α : impact angle (°)

δ : impact direction (°)

θ : inclination angle (°)

φ : azimuth angle (°)

Subscript/Superscript Description

\wedge : normalized value

\perp : perpendicular component

\parallel : tangential component

X : component or plane associated with the X-direction

Y : component or plane associated with the Y-direction

Z : component or plane associated with the Z-direction

RESUMEN

En flujos turbulentos, el desgaste erosivo es causado por impactos de partículas desviadas del flujo nominal por la acción de las fluctuaciones turbulentas. Así, la topografía de la superficie durante el proceso de erosión contiene información significativa sobre la extensión del desgaste erosivo, como lo son la profundidad de los cráteres y el volumen de material removido. Esta investigación describe una determinación experimental de la distribución del ángulo de impacto y del ángulo de direccionalidad mediante un análisis de imágenes de zonas desgastadas, así como un procedimiento de análisis inverso para la determinación de la velocidad de impacto de partículas mediante información de perfilometría 3D y modelación.

Se utiliza la configuración *slurry pot* para producir daños por desgaste en una pieza de cobre al exponerse al flujo de microesferas de vidrio de baja concentración. La degradación se evalúa mediante la pérdida de peso, y los datos topográficos para el análisis de la imagen se obtienen mediante perfilometría 3D. El modelado se lleva a cabo a través de dos modelos empíricos (Oka y Huang) y un modelo teórico (Cheng).

Los resultados revelan que la mayor parte de la energía cinética es transferida por la componente tangencial de la velocidad de impacto dado por bajos ángulos de impacto, independientemente del tamaño de partícula. Las condiciones de impacto de partículas no distribuyen *normal* y se establece estadísticamente un ángulo de impacto máximo para la configuración *slurry pot*. Además, la velocidad calculada puede diferir mucho según el modelo utilizado, donde los modelos Huang y Cheng están más cercanos a las condiciones de flujo nominal que el modelo Oka. Finalmente, se explora el grado de correlación monótonica entre las variables experimentales para marcas erosivas individuales.

Palabras Claves: Erosión, Ángulo de impacto, Velocidad de impacto, Flujo turbulento, Análisis de imágenes, Análisis inverso.

ABSTRACT

In turbulent flows, erosive wear is given by particle impacts deviated from nominal flow by turbulent fluctuations. Thus, surface topography after slurry erosion contains meaningful information concerning the extent of erosive wear, such as indentation depth and wear volume. This research describes an experimental determination of particle impact angle and impact direction distributions from collective wear scar features by image analysis, as well as a procedure of inverse analysis for the determination of particle impact velocity from collective erosive features by means of further modeling.

Slurry pot is used to produce wear damage on copper in exposure to highly turbulent dilute slurry flow of glass beads. Degradation is evaluated by weight loss, and topography data for the image analysis is acquired by non-contact 3D profilometry. Modeling is carried out through two empirical models (Oka and Huang) and one theoretical model (Cheng).

The results reveal that most of the kinetic energy is transferred by the tangential component of the impact velocity at shallow impact angles, regardless the particle size. Particle impact conditions do not distribute Gaussian and a statistical cut-off angle is established. Additionally, the back-calculated velocity may greatly differ depending on the model used, where Huang and Cheng models are closer to the nominal flow conditions than the Oka model. Finally, the degree of monotonic correlation between experimental variables for individual erosive features is explored.

Keywords: Slurry erosion, Impact angle, Impact velocity, Turbulent flow, Slurry pot, Image Analysis, Inverse analysis.

LIST OF PAPERS

Molina, N., Aguirre, J., & Walczak, M. (2019). Application of FFT analysis for the study of directionality of wear scars in exposure to slurry flow of varying velocity. *Wear*, 426, 589-595.

Molina, N., Walczak, M., & Michalczewski, R. (2020). Erosion under turbulent slurry flow: An experimental determination of particle impact angle, impact direction, and distribution thereof by image processing. *Wear*, 203302.

1. INTRODUCTION

Slurry erosion is the process of the degradation of a material by wear caused by the impact of incoming particles from the carrier gas or liquid phase. In many industries, this process may include complex phenomenon due to the electrochemical interaction of the carrier fluid with the target surface, leading to an erosion-corrosion synergy found in a wide variety of sectors: marine, oil and gas, nuclear, high temperature, power generation, mining, manufacturing, and process industry (Burson-Thomas & Wood, 2017; Javaheri, Porter, & Kuokkala, 2018; Kuruvila, Kumaran, Khan, & Uthayakumar, 2018). In the past decade, the effort of the researchers has been mainly focused on testing and protection of materials, highlighting particularly modeling for the development and validation of models for predicting wear rate. These models have become very useful for improving the design of gas- and hydro-components through computational fluid simulations (Burson-Thomas & Wood, 2017; Messa & Malavasi, 2017).

In the case of particles carried by a liquid phase, it has been well established by numerous experiments that the extent of wear by slurry erosion depends on the properties of the impacting particles (size, shape, density, and hardness), carrier liquid (particle concentration, viscosity, temperature, and density), and target material (microstructure, ductility, and hardness) (Burson-Thomas & Wood, 2017; Javaheri et al., 2018; Kuruvila et al., 2018). However, the particle impact characteristics given by the flow such as impact velocity (or kinetic energy) and impact angle are the most prominent parameters correlated with the wear rate (Kuruvila et al., 2018). This is particularly challenging to describe in highly turbulent flows, where the modification of the particle trajectories and velocities due to turbulent fluctuations, coherent turbulent structures, and eddy currents may determine the overall wear not only by each particle's motion but also their statistics (Ma et al., 2015).

As it was reported by Wang et al. (Huakun Wang et al., 2019), to date, more than 200 erosion models have been proposed (Parsi et al., 2014; S. M Hsu, 1997). From these models, only a few are considered practically important, amongst which the DNV (D.N. Veritas, 2011), E/CRC (Zhang, Reuterfors, McLaury, Shirazi, & Rybicki, 2007), Finnie

(Finnie, 1960b), Huang (Huang, Chiovelli, Minev, Luo, & Nandakumar, 2008), and Oka (Oka, Okamura, & Yoshida, 2005; Oka & Yoshida, 2005) erosion equations are the most widely used owing to their numerous experimental validation, especially for common steel grades (Javaheri et al., 2018; Messa & Malavasi, 2017; Njobuenwu & Fairweather, 2012). In addition to the empirical or semi-empirical formulations, from the theoretical point of view, there has been progress in the development of analytical and phenomenological erosion models for single impacts for elastic-plastic materials with strain hardening, even considering frictional effects (Brake, 2015; I. A. Lyashenko, 2019; Iakov A. Lyashenko, Willert, & Popov, 2018; Hui Wang, Yin, Hao, Chen, & Yu, 2020; Willert, 2019).

Observation of the worn surface morphology and topography produced during exposure to solid particle erosion is known to be indicative of the damage mechanism (cutting, ploughing, abrasion, etc.) associated with the particle impact conditions (Javaheri et al., 2018; Shitole, Gawande, Desale, & Nandre, 2015). In previous studies, the experimental characterization of the particle impact angle after exposure has been addressed only to illustrate a single wear scar depth profile from a cluster of erosive features (Alam & Farhat, 2018; Andrews, Giourntas, Galloway, & Pearson, 2014; Frosell, Fripp, & Gutmark, 2015; Nguyen et al., 2019, 2014), i.e. it has been explored for an individual feature rather than collective, lacking the statistical perspective. Only recently, a collective and statistical point of view was proposed to study the evolution of the impact direction (directionality) distribution in connection with increasing velocity, but no information was given about the impact angle distribution (Molina, Aguirre, & Walczak, 2019). Thus, to our best knowledge, the issue of the deconvolution of particle impact direction and impact angle distributions from collective erosive features after exposure to turbulent slurry flow has not been addressed systematically in the literature.

On the other hand, the experimental characterization of local impact diameter, indentation depth or wear volume have been addressed, however, from these variables have been few attempts to acquire statistical data of the slurry flow conditions that caused the material degradation with no prior knowledge of the erosive flow set-up (Hector Mc I. Clark, 1991; Hutchings, 1981; Ma et al., 2015). Hence, to our best knowledge, the issue of the inverse analysis of the particle impact velocity statistics from single to collective

erosive features after exposure to turbulent slurry flow has not been addressed systematically in the literature.

In this context, the first aim of this work is to quantify the impact angle and impact direction distributions of wear scars in highly turbulent flow at different particle sizes by the means of image processing and analysis in order to elaborate on the relationship between impact conditions and particle kinetic energy. In this research, a copper target is exposed to dilute slurry erosion by means of a slurry pot system using glass bead particles of various sizes covering the range of reportedly inducing erosive damage (H. Mc I. Clark & Hartwich, 2001a; H. McI Clark, 2002; Hadavi, Moreno, & Papini, 2016; Lynn, Wong, & Clark, 1991; Telfer, Stack, & Jana, 2012; Thakare, Wharton, Wood, & Menger, 2012; Tressia, Penagos, & Sinatora, 2017). The worn surfaces are analysed by non-contact 3D profilometry and processed by image analysis techniques for interpretation.

The second focus of the current work is to determine the statistical particle impact velocities in a worn surface by observing the topography of wear scars produced in highly turbulent slurry flow. The inverse analysis procedure consists of the digitalisation of topography and further modeling of localised deformation. Particle erosion models are back solved to deconvolute the particle impact velocity of each wear scar. This methodology was applied to two well-known empirical models: Oka and Huang, commonly used in the engineering practice (Huang et al., 2008; Oka et al., 2005; Oka & Yoshida, 2005). In addition, a theoretical elastic-plastic model proposed by Cheng *et al.* (Cheng, Zhang, Wei, Mi, & Dou, 2019) was used, which provided the comparison between empirical equations with recent theoretical models. Finally, the effectiveness and limitations of the inverse analysis methodology are discussed.

2. LITERATURE REVIEW

The following literature review has been limited to erosion only, although there are other wear mechanisms that can be observed jointly as the product of slurry erosion phenomenon, such as corrosion and/or cavitation (Grobler & Mostert, 1990; Madsen, 1988).

2.1. Slurry erosion

2.1.1. Fundamentals of erosion mechanisms

Solid particle erosion is the process of material removal that occurs when discrete solid particles strike a surface, this generates the progressive loss of material, which can be removed by plastic deformation and/or brittle fracture, depending on the material being eroded away and on the operating conditions (Rohatgi, Tabandeh-Khorshid, Omrani, Lovell, & Menezes, 2013). In particular, if the incoming particles are carried by a liquid phase, this process is called slurry erosion (Javaheri et al., 2018).

Slurry erosion is a complex, time-dependent phenomenon that has been systematically investigated for the first time in the 1960s (Bitter, 1963; Finnie, 1960a). Since then erosion has been assumed to occur due to two main mechanisms, referred to as “cutting” and “deformation”, which are terms not related to their usual meaning in metallurgy (Finnie, 1960a). The “cutting” mechanism is associated with low impact angles with enough kinetic energy to cut the material by the erodent like a knife or cause by ploughing the formation of ripples and lips that can be further chipped away from the surface after subsequent impact or flow momentum transfer (Uzi & Levy, 2018), as it is shown in Fig. 1.

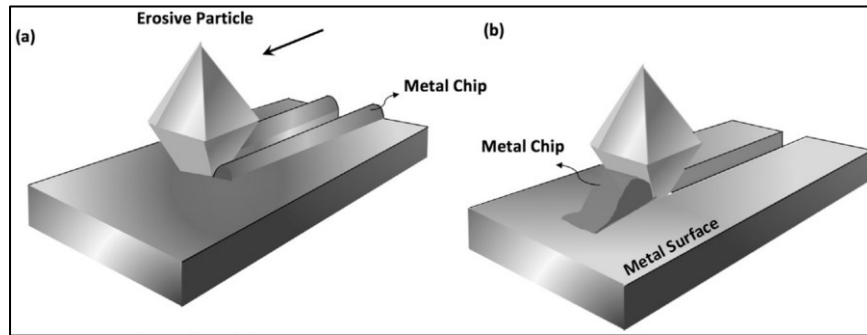


Figure 1. Schematic illustration of a) ploughing and b) cutting erosion mechanism.

Adapted from (Javaheri et al., 2018).

On the other hand, the “deformation” mechanism is associated with high impact angles with enough kinetic energy to cause plastic deformation or subsurface crack formation leading to fracture in the eroding surface (Hector McI. Clark & Wong, 1995). Both mechanisms are illustrated in Fig. 2 for ductile and brittle target materials.

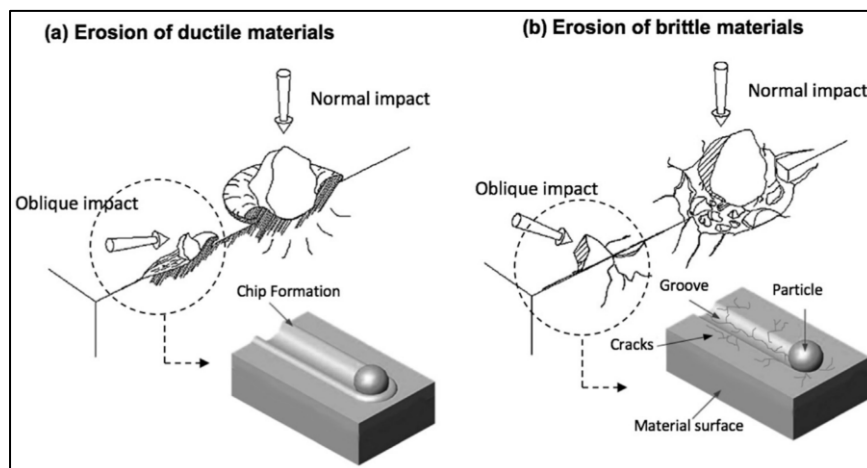


Figure 2. Schematic representation of erosion caused by deformation mechanism at normal impact and cutting mechanism at oblique impact in a) ductile and b) brittle materials (Y.

F. Wang & Yang, 2008).

According to Uzi & Levy (2018), the initial kinetic energy before particle impact is the sum of the particle's translational and rotational energies. During the impact, energy is absorbed by the particle or eroding surface, which leads to lower kinetic energy when the particle bounces off the wall due to energy loss. Then, the energy conservation equation before and after the impact reads (Eq. 1):

$$E_{k,i} + E_{\omega,i} = E_{k,R} + E_{\omega,R} + E_p + E_w + W \quad (1)$$

where E_k and E_ω are the translational and rotational kinetic energy, respectively; i and R subscripts denote the initial and rebound states, respectively; E_p and E_w are the energies absorbed by the particles or eroding surface, respectively. In particular, W is the energy dissipation by stress waves.

Based on experimental results, both the stress waves (Hutchings, 1979) and the difference of the rotational kinetic energy (Hutchings, 1976; Walley & Field, 1987) have been found to be much smaller than the initial energy, and therefore, both terms are considered negligible. The energy absorbed by the eroding surface is divided into the aforementioned two mechanisms: cutting (EC) and deformation (ED), which are assumed to be controlled by the kinetic energy associated with the tangential and normal components of the velocity, respectively. The energy absorbed by the particle cause plastic deformation of the particle, crack developments, and fracture (Uzi & Levy, 2018), although to simplify the erosion modeling, it is assumed a rigid particle. Then, considering the above assumptions, the simplified energy exchange can be rewritten as Eqs. 2 and 3:

$$\Delta E_{k,t} = E_C \quad (2)$$

$$\Delta E_{k,n} = E_D \quad (3)$$

It has to be remarked that these mechanisms operate simultaneously at any angle that differs from a perpendicular collision (E_D pure case), although, depending on the impact conditions and material properties, one may predominate (Javaheri et al., 2018). In the case of low impact angles, cutting and ploughing may differ from the abrasion

phenomenon at least in two aspects: collision contact time is much shorter in erosion than abrasion (Shitole et al., 2015), and abrasion damages the surface due to the passage of particles over the surface but without impingement; nevertheless, these mechanical wear processes display many similarities (Truscott, 1972).

2.1.2. Fundamentals of erosion mechanisms

Javaheri *et al.* (2018) summarize the principal parameters contributing to slurry erosion by classifying them into four groups: slurry characteristics, target material properties, solid particle properties, and impingement condition; as schematically shown in Fig. 3. These are discussed below.

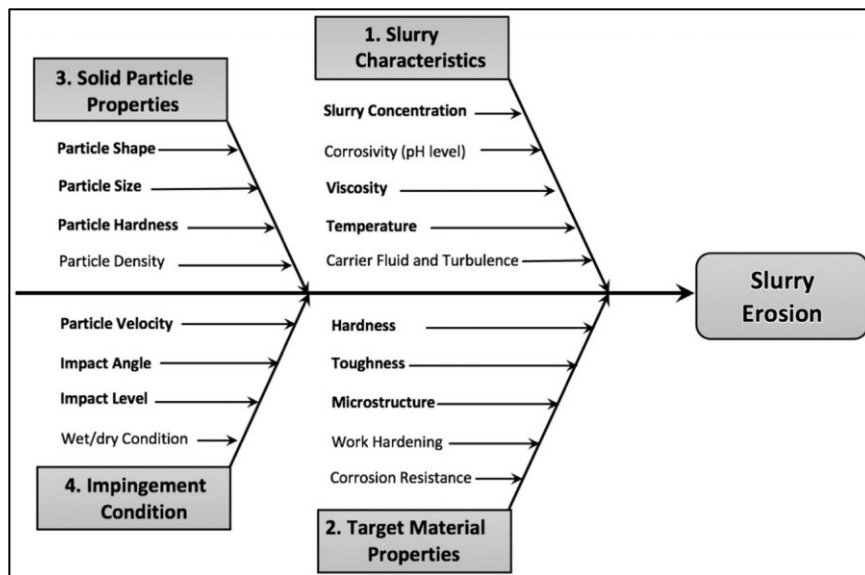


Figure 3. Fishbone of important parameters influencing slurry erosion (Javaheri et al., 2018)

a) Slurry characteristics

In less viscous carrier fluids, such as water, higher particle concentration in the slurry leads to a higher erosion rate due to the increasing number of particles striking the target material (Gandhi, Singh, & Seshadri, 1999; Tsai, Humphrey, Cornet, & Levy, 1981), and settlement of particles which produces a sliding bed, as it has been observed in slurry pipelines, especially for particles with higher density (Mansouri, Shirazi, & McLaury, 2014).

b) Target material properties

Among the many material properties affecting surface degradation: microstructure and average mechanical properties are distinguished.

Microstructures consist of different phases with differing physical and mechanical characteristics, which could lead to localized damage, as pointed out by many researchers (Al-Bukhaiti, Ahmed, Badran, & Emara, 2007; Alam, Aminul Islam, & Farhat, 2015; Islam, Alam, Farhat, Mohamed, & Alfantazi, 2015; Okonkwo, Mohamed, & Ahmed, 2015). For example, in the case of ductile ferritic-pearlitic steel microstructures, it has been found that the pearlite phase is more effective in resisting ploughing, cutting and deformation than ferrite; even more, the damage could also depend on the orientation of the cementite lamellae relative to the impact directionality (Alam et al., 2015; Islam et al., 2015).

On the other hand, while it is generally believed that increasing hardness reduces the erosion (Oka, Matsumura, & Kawabata, 1993; Oka et al., 2005), as it is shown in Fig. 4, others suggest that other mechanical properties should also be considered (Hussainova, Kubarsepp, & Pirso, 2001; Oka & Yoshida, 2005; Sheldon, 1977) due to contradictory results in studies related to hardness (Levy, 1981; O'Flynn, Bingley, Bradley, & Burnett, 2001). For instance, toughness and yield stress are considered as relevant as hardness in the study of erosion, since the loss of ductility

(hardening) may increase the erosion rate through a brittle mechanism (Naim & Bahadur, 1986; Sheldon, 1977).

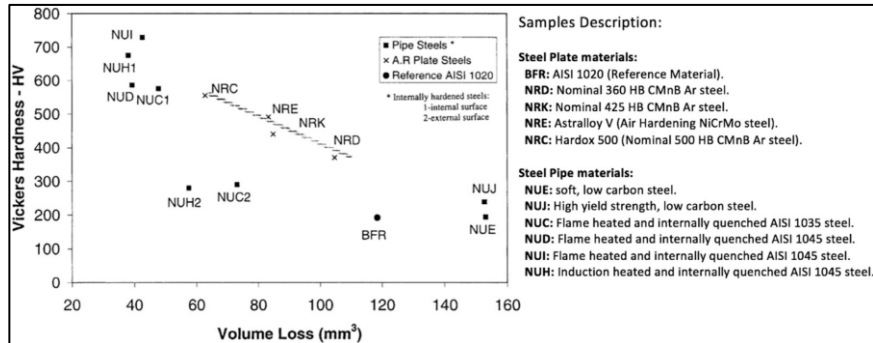


Figure 4. Volume loss and average near-surface hardness data for steel plate and steel pipe materials (H. M. Clark & Llewellyn, 2001).

c) Solid particle properties

Among the many solid particle properties affecting the surface degradation are shape, size, and hardness (Abouel-Kasem, 2011; H. Mc I. Clark & Hartwich, 2001b; Liebhard & Levy, 1991; Walker & Hambe, 2015; Yabuki, Matsuwaki, & Matsumura, 1999).

Particle shape is customarily classified as one of the two main categories: angular and rounded, in which the former causes more damage than the latter (Levy & Chik, 1983). This factor has been quantified by means of circularity, which is unity for a perfect circle and zero for an infinite elongated polygon. In Table 1 and Fig. 5 are presented some of the frequently used erodents in industry.

Table 1. Properties of frequently used erodent particles (Javaheri et al., 2018).

Erodent particles	Hardness (HV, GPa)	Density (g/cm ³)	Shape
Alumina (Al ₂ O ₃)	1.8	3.94	Angular
Silicon Carbide (SiC)	2.5	3.22	Angular
Quartz (SiO ₂)	0.75	2.65	Fairly rounded
Glass Beads	0.6	2.6	Spherical
Tungsten Carbide	2.2	15.7	Irregular
Diamond	8	3.5	Blocky

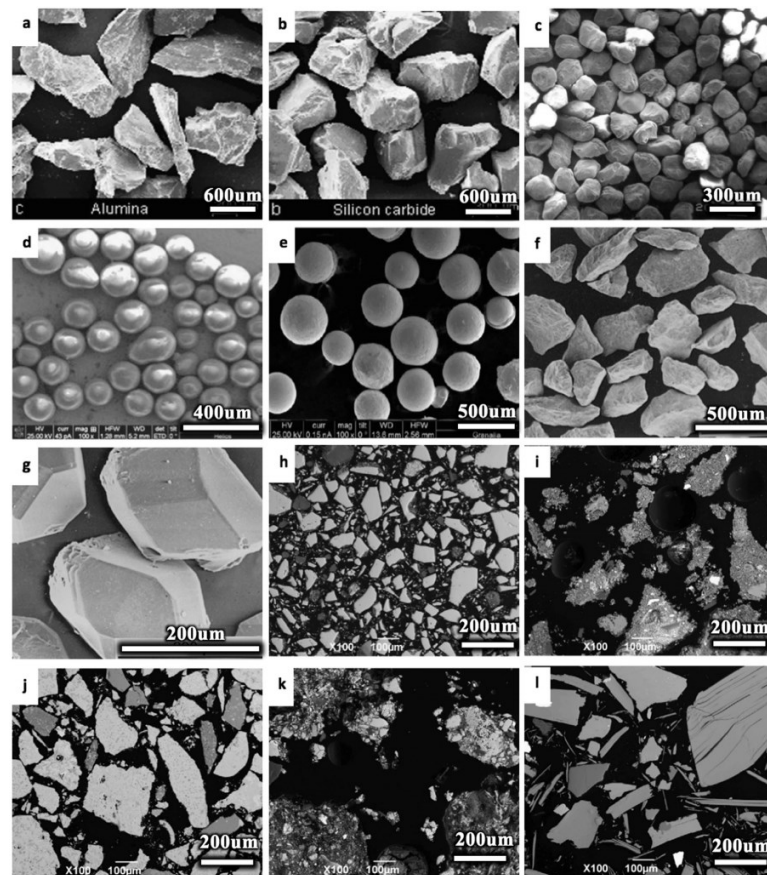


Figure 5. SEM images of a) alumina, b) silicon carbide, c) quartz, d) glass beads, e) steel round grit, f) tungsten carbide, g) diamond, and cross-section SEM images of h) chromite, i) concentrate, j) matte, k) ore, and l) tailings. Retrieved from Javaheri et al. (2018).

Regarding the particle size effect, if the particle size increases at a constant velocity, the particles acquire more kinetic energy, causing greater damage at the impact (Parsi et al., 2014; Sinha, Dewangan, & Sharma, 2017). In addition, with an increase in the ratio of the erodent particle hardness to the target material hardness, the total erosion increases until a threshold value after which this relationship has little effect (Levy & Chik, 1983).

d) Impingement condition

In order to cause damage by an impacting particle, the impact velocity should be above a threshold below which no plastic deformation is produced, i.e., the collision should not be a purely elastic one (Yabuki et al., 1999). However, this factor it is not only related to the transfer of kinetic energy but to the contact stress at the impact as well (Y. F. Wang & Yang, 2008).

On the other hand, both ductile and brittle material have a characteristic impact angle curve, which is mostly due to the shift in the wear mechanism discussed in Section 2.2.1. Figure 6 shows typical examples of impact angle dependence.

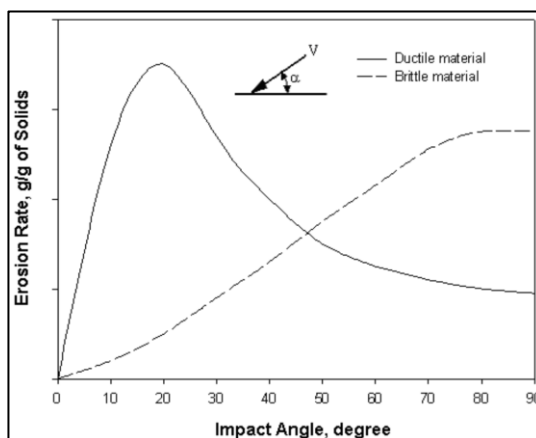


Figure 6. Variation of erosion rate with impact angle for brittle and ductile materials (Nandre & Desale, 2018)

2.2. Erosion modelling

From the models considered practically important, both DNV and E/CRC have not determined the experimental coefficients of their models for copper as target material. In Finnie's model, the cutting and deformation energy factors are not constant for varying impact angles and should be measured (Biswas, Williams, & Jones, 2018). In contrast, Huang and Oka models have validated their models for copper. Furthermore, both have used sandblast type erosion rig to develop their experimental coefficients, i.e., the results came from collective and successive particle impacts, which is relevant because both are in practice used for calculation of single impact wear in CFD simulations (Messa & Malavasi, 2017).

From the theoretical point of view, the phenomenological models with explicit physical significance are complex to deal with. However, recently a theoretical formulation derived by Cheng et al (Cheng et al., 2019) showed good agreement to experimental results without involving too many physical coefficients.

Hence, in this work, three models are studied: Huang, Oka, and Cheng. Each of these models is described in the following subsections.

2.2.1. Oka model

The Oka model has been a widely used erosion model for wear prediction (Messa, Mandelli, & Malavasi, 2019; Pereira, de Souza, & de Moro Martins, 2014; Zheng et al., 2019). The wear volume equation ($mm^3/impact$) is written as:

$$E_V = m_p E_R \quad (4)$$

$$E_R = K(aH_w)^{k_1 b} \left(\frac{\|V\|}{V'}\right)^{k_2} \left(\frac{d_p}{D'}\right)^{k_3} f(\alpha) \quad (5)$$

$$f(\alpha) = \sin^{n_1}(\alpha) [1 + H_w(1 - \sin(\alpha))^{n_2}] \quad (6)$$

where m_p is the particle mass, H_w is the hardness of the target material, $\|V\|$ is the particle speed, d_p is the particle size, and α is the impact angle. K , k_1 , k_2 , k_3 , n_1 , n_2 are

empirical constants that are related to the properties of both particles and target. V' and D' are a reference particle velocity particle size. a and b characterize the load relaxation ratio of the target material, usually taken to be unity in the lack of experiments.

2.2.2. Huang model

The Huang model incorporates the removal of material due to both deformation damage and cutting, following the work done by Finnie and Bitter. The simplified wear volume equation ($mm^3/impact$) is written as:

$$E_V = C m_p \rho_p^{0.15} (\|V\| \sin(\alpha))^{2.3} + D m_p^{1.1875} d_p^{-0.0625} \|V\|^{2.375} \cos^2(\alpha) \sin^{0.375}(\alpha) \quad (7)$$

where ρ_p is the particle density, and m_p , $\|V\|$, α , d_p have the same meanings as in Eqs. (1-3).

2.2.3. Cheng model

The Cheng model is derived from elastic-plastic assumptions in the Hertzian contact between the erodent and target material. It develops independent equations for the calculation of the indentation depth and wear scar length. The simplified indentation depth equation ($m/impact$) is written as:

$$\frac{m_p}{2} V_{\perp}^2 = \left(\frac{1}{2} Y_w \pi r_p \right) h^2 + \left(0.17 \cdot \frac{Y_w^3 \pi^2 r_p^2}{E_{eff}^2} \right) h \quad (8)$$

where V_{\perp} is the normal velocity component, Y_w is the yield strength of the target material, r_p is the particle radius, h is the indentation depth, and E_{eff} is the effective Young's modulus. The particle speed can be retrieved from the trigonometric definition:

$$\|V\| = \frac{V_{\perp}}{\sin(\alpha)} \quad (9)$$

2.3. Image processing

In this section, it is not reviewed the use of characterization techniques such as Scanning Electron Microscopy (SEM) or Interferometry used in the context of erosion wear, because although both techniques are widely employed in the literature (Abd-Elrhman, Abouel-Kasem, Ahmed, & Emara, 2014; Islam & Farhat, 2014; Kosa & Göksenli, 2015; Nguyen et al., 2014; Shitole et al., 2015), usually they are not further treated with an image processing technique.

In the slurry flow studies, there are few attempts to use image processing techniques to acquire further information from the worn surfaces. For instance, to our best knowledge, the issue of distribution of directionality of erosion wear scars has not been addressed systematically in the literature, except for a manual indication of erosion tracks (Ranjbar, Ghasemi, & Abedini, 2015) and divergence of particle impacts (Abd-Elrahman, Abouel-Kasem, Ahmed, & Emara, 2014). Our exploratory study (Molina et al., 2019) followed the hypothesis that directionality of erosive scars contains indirect information on the orientation of particle impact and the directionality can be assessed in a holistic manner, i.e., all scars analyzed at once, by means of image processing based on Fourier transformation. The main premise was that worn surfaces can be interpreted as a two-dimensional function in the spatial domain, containing both periodic and irregular elements, as well as noise and background. Difficulty in visual inspection of such features in erosive damage increases with damage accumulation because the above-named image components are commonly embedded and entangled with one another.

In particular, Fast Fourier transform (FFT) translates the image form the spatial domain into a two-dimensional complex function in the frequency domain, enabling differentiation of original features by their spatial frequencies (Wood, 1990; Xu, 1996). The square of the function's magnitude, i.e. its power spectrum, is displayed against frequency to visualize the contribution of each frequency to the FFT and, in case of 2D images, allows identifying preferential directionality of patterns if any were present in the spatial domain. Applicability of FFT for observing and analyzing information not easily extracted in the spatial domain has been shown effective for a variety of applications such as assessing woven fabric structures (Xu, 1996), collagen architecture (Osman et al.,

2013), alignment of electrospun fibers (C. Ayres et al., 2006; C. E. Ayres et al., 2007, 2008; Shang, Yang, Cheng, Frank Walboomers, & Jansen, 2010) or alignment of nanotubes in a membrane (Omar et al., 2015). Thus, as of the date the use of FFT image analysis has been first reported by us in the context of erosive wear.

For example, from this work is concluded that the technique of FFT employed to SEM generated images of wear scars is applicable for meaningful identification of symmetries in the wear scar patterns. For increasing nominal flow velocity in the system of rotating cylinder, i.e., rotation frequency, evolution of directionality in the wear scars pattern was identified (Fig. 7), which is indicative of the condition of turbulence.

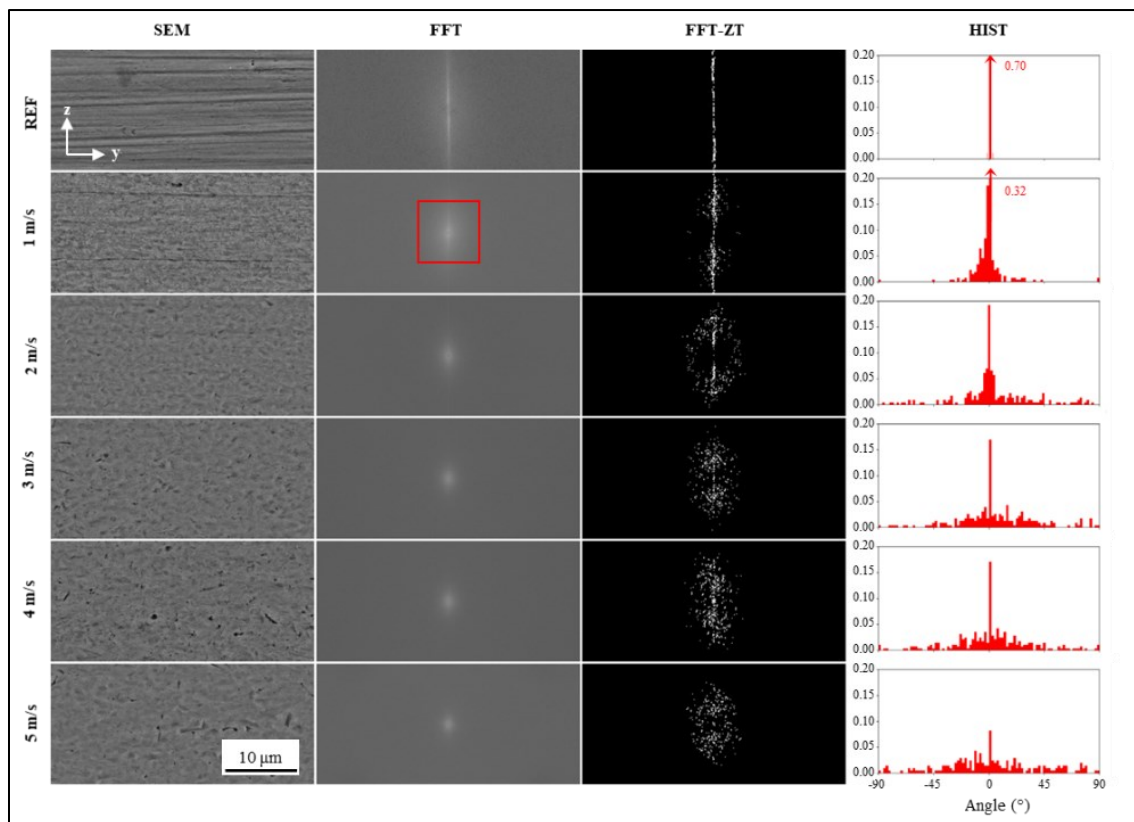


Figure 7. Image analysis for SEM micrographs obtained for different flow velocities: FFT – fast Fourier transform, FFT-ZT – contrast adjusted visualization of selected FFT zone (red rectangle), HIST – histogram of wear scar orientation (δ) as determined by image analysis of FFT-ZT (Molina et al., 2019)

Finally, a special mention should be done to the image processing work related to the erodent, as it was reviewed by Raadnui (2005) and shown in Table 2. Recently, some advancements in wear debris identification (Cao, Zhang, Wang, Wang, & Peng, 2019), especially using neural networks (S. Wang, Wu, Shao, & Peng, 2019) have shown a new direction in the community to use these tools.

Table 2. Particle shape and size descriptors relevant for wear (Raadnui, 2005).

Method	Attribute	Descriptor	Abbreviation	Definition
Form factor	Profile	Aspect ratio Roundness factor	AR RF	Length/Breadth (Perimeter) ² /4π(Area)
Fourier analysis	Profile and edge detail	1st, 2nd, ..., harmonics	C_1, C_2, \dots, C_8 $\mu_0, \mu_1, \mu_2, \mu_3$	$C_n = \sqrt{(Cx_n^2 + Cn^2)}$ $R_0 = a_0^2 + \frac{1}{2} \sum_{n=1}^8 (a_n^2 + b_n^2)$ $\mu_0 = L_0 R_0, \mu_1 = 0$ $\mu_2 = R_0^2 \sum_{n=1}^8 L_{2,n}$ $\mu_3 = R_0^3 \sum_{n=1}^8 \sum_{m=1}^8 L_{3,m,n}$
Curvature analysis	Edge detail	Standard deviation Skewness Kurtosis	R_q R_{sk} R_{ku}	$R_q = \sqrt{\sum_{i=1}^n (x_i - \bar{x})^2 / n - 1}$ $R_{sk} = \sum_{i=1}^n (x_i - \bar{x})^3 / n R_q^3$ $R_{ku} = \sum_{i=1}^n (x_i - \bar{x})^4 / n R_q^4$
Fractal analysis	Edge detail and profile	Structure Texture	δ_s δ_T	$\delta_s = 1 + m_s $; m_s is slope of the line of best fit from the plot of log normalized perimeter vs. log step length (large step length) $\delta_T = 1 + m_T $; m_T is slope of the line of best fit from the plot of log normalized perimeter vs. log step length (very small step length)
Size analysis	Size	Weibull parameter	α β	$P(\chi) P(\chi) = 1 - \exp\left\{-\left(\frac{\chi-\chi_0}{\alpha}\right)^\beta\right\}$

3. THESIS PROPOSAL

3.1 Hypothesis

The leading hypothesis of the proposed research is that in erosion by slurry flow, the distribution of particle impact characteristics (impact angle, impact direction, and impact velocity) can be quantified by means of image processing of wear scars from a ductile material exposed to a highly turbulent flow. In particular, it hypothesized that the information obtained from worn surfaces analysed by non-contact 3D profilometry allows identifying the particles' impact conditions without prior information.

3.2 General objective

The general objective of this research is to quantify the correlation between the particle size and the impact characteristics (impact angle, impact direction, and impact velocity) established in the exposure of copper to dilute slurry erosion as determined in a slurry pot system, with a particular interest in the statistical behavior of the turbulent flow.

3.3 Specific objectives

The following specific objectives reflected in the methodology are to be pursued:

- I. Implement an experimental design and procedure to generate wear scars in a copper target material mounted in a slurry pot system.
- II. Quantify the impact characteristics (impact angle and impact direction) by means of image processing of the 3D topography of the worn surface.

- III. Estimate the impact velocity by means of an inverse analysis of erosion models and topography data.
- IV. Determine the correlation of the impact characteristics, particle size, and wear rate associated to the collective features of the worn surface.

4. EXPERIMENTAL

4.1 Sample preparation

The material for the study was Electrolytic Tough Pitch Copper C11000 (Cu-ETP) hardened by cold working (H04 ASTM) and of a chemical composition determined by glow discharge emission spectrometry bulk analysis (Spectrums, GDA 750 h): Zn 0.001%, Si 0.001%, Fe 0.001%, and Cu balance (all values in wt.%). The measured properties of Cu-ETP are reported in Table 3:

Table 3. Physical and mechanical properties of Cu-ETP used in this study.

Density (g/cm ³)	8.9
Rockwell hardness (F)	85
Vickers hardness (GPa)	0.99
Yield strength (MPa)	275
Young's modulus (GPa)	94
Poisson ratio	0.33

Cylinders of 15 mm in diameter and 10 mm in height were prepared by machining a Cu-ETP bar. The machining parameters were those recommended by ASTM (see Supplementary Material, Table S1). The curved surface of the cylinder was polished by means of four steps described in Table 4. The final surface roughness (Sa) was about $0.05 \pm 0.02 \mu\text{m}$.

Table 4. Details of the processes used for surface finish prior exposure.

<i>Process</i>	<i>Abrasive/Physical agent</i>	<i>Tool</i>	<i>Parameters</i>
Uniform polishing	SiC paper (600 down to 3000 grit)	Lathe turning machine	2000 RPM
Final polishing	PCD suspension (3 and 1 μm)	Lathe turning machine	300 RPM
Final polishing	Silica colloidal suspension (0.04 μm)	Lathe turning machine	300 RPM
Electropolishing	Phosphoric acid (H_3PO_4) 15 M	Cu-ETP as cathode	1.6 V, 5 min.

Finally, the samples were rinsed and sonicated in acetone, dried by blowing hot air and stored in a desiccator for use in the experiment. The weight of each sample was measured using an analytical balance (Sartorius BP221S) with a precision of 0.1 mg.

4.2 Erodent preparation

The erodent used in this study were glass beads of measured properties reported in Table 5:

Table 5. Physical and mechanical properties of the glass beads.

Density (g/cm^3)	2.5
Vickers hardness (GPa)	6.2 ± 0.5
Young's modulus (GPa) ^a	72.2
Poisson ratio ^a	0.168
Circularity ^b	0.82

^a Retrieved from (Pabst & Gregorová, 2013).

^b Circularity was obtained from ~200 particles through analysis of SEM images employing ImageJ (Rueden et al., 2017).

In order to study the effect of particle size, the erodent was sieved in five mesh ranges, giving a selected particle size distribution reported in Table 6. The smallest particle size was chosen so that the wear scar imprint might be well characterized by the lateral resolution of the profilometer (Section 2.5.1). It should be kept in mind that, in the remaining text, the particle size (d_p) refers to the midrange value.

Table 6. Particle size ranges used in this study.

Mesh US	Particle size range (μm)	Midrange particle size (μm)
20-25	707-841	774
25-30	595-707	651
30-35	500-595	548
35-40	400-500	450
50-60	260-297	276

The shape of the particles as observed under a scanning electron microscope (SEM) is shown in Figure 8.

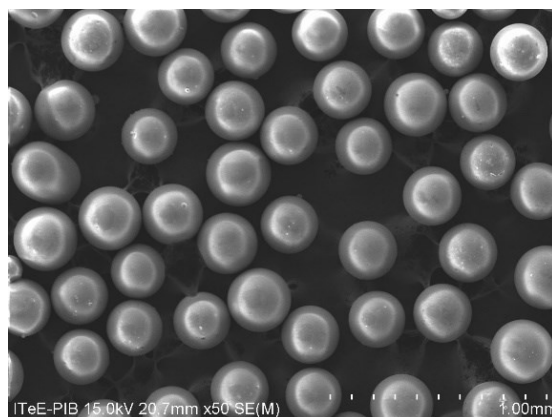


Figure 8. A representative shape of glass beads (50-60 mesh, d_p of 276 μm) observed under SEM. For other mesh sizes see Figure 28 in Appendix B.

4.3 Experimental rig

Experiments were carried out using a slurry pot. Figure 9 shows the configuration of the experimental system, consisting of a motor controlled by a frequency modulator connected to a rotating shaft, to which one cylindrical sample (Section 2.1) is mounted in the lower part and exposed to a tangential flow of slurry. The shaft is immersed in the slurry container made of acrylic (\varnothing 70 mm) that is filled with a total volume of 300 mL. Four baffles are mounted at 90° to avoid sedimentation at the bottom. The concentricity of the shaft and sample is ensured by a cylindrical pivot bearing at the bottom of the slurry container, which efficiently reduces vibration. The rig does not allow for direct control of the angle at which the particles hit the surface, which is determined by the conditions of the flow.

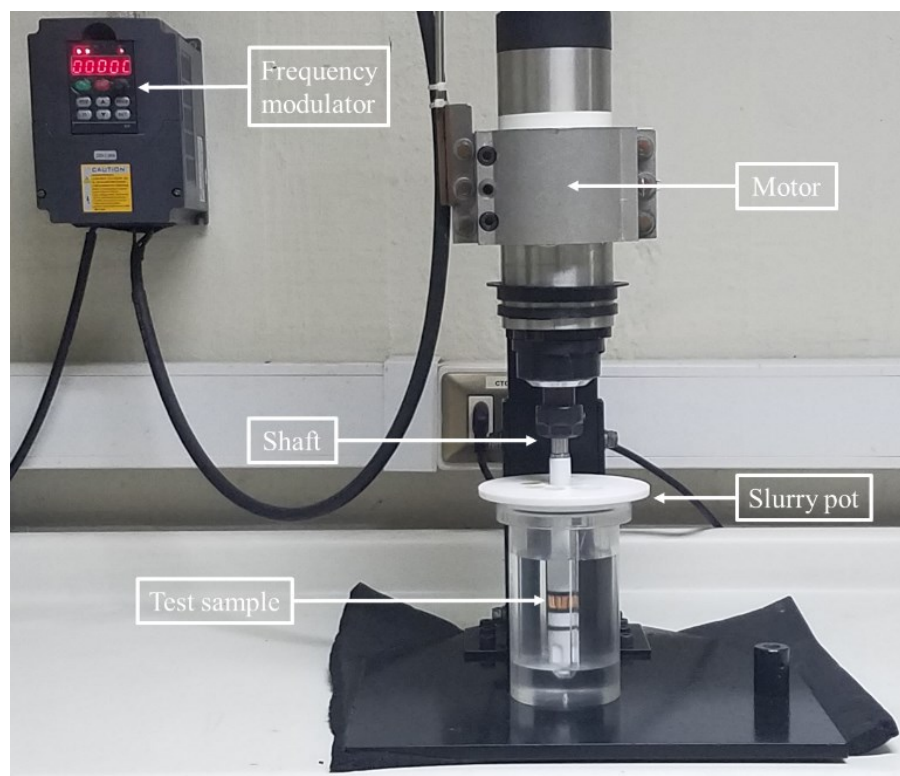


Figure 9. Overview of the experimental set-up. For better visibility of the test samples, the pot is filled with water instead of slurry.

4.4 Experimental procedure

The experiments were performed using distilled water (5.7 pH, 25±1 °C). The number of particles for every particle size range was kept constant at about 12,500 particles by adjusting the slurry concentration depending on the particle size range at the given total volume of 300 mL, summarized in Table 7. The slurry was not intervened during exposure.

Table 7. Slurry concentration for different particle sizes.

<i>Particle size (μm)</i>	<i>Mass per test (g)</i>	<i>Solid weight fraction (wt.%)</i>	<i>Solid volume fraction (vol.%)</i>
774	7.500	2.463	1.000
651	4.463	1.487	0.595
548	2.655	0.880	0.354
450	1.474	0.490	0.197
276	0.338	0.112	0.045

The concentration of glass beads was very low (<1 vol.%) to neglect particle-particle interaction (Humphrey, 1990) and to ensure a surface with the first imprints of the impact features. In each exposure run, the sample was mounted in the same position to assure its reproducible condition with respect to the height of the slurry. The frequency of rotation was fixed for the different exposure runs to produce the desired value of 10 m/s linear speed at the tangential surface of the test cylinder. However, this nominal linear velocity is not necessarily acquired by each particle because of the turbulence. The Reynolds numbers estimated after Grossmann et al. (Grossmann, Lohse, & Sun, 2016) at the gap and the shaft are about 274,000 and 75,000, respectively. In addition, the high value of the Taylor number characteristic of the set-up and materials, about $1.78 \cdot 10^{12}$, ensures that the formation of stable coherent structures, such as Taylor rolls, are not promoted in the test rig.

On the other hand, according to Israel and Rosner (Israel & Rosner, 1983), in a turbulent flow, the conventional Stokes number overestimates the tendency of particles to deviate from the nominal flow direction because the drag force is underestimated. Thus, a generalized Stokes number would be more appropriate.

Table 8 summarizes the theoretical kinetic energy acquired per particle and the generalized Stokes number estimated by assuming that the nominal flow velocity was acquired by each particle.

Table 8. Theoretical kinetic energy of erodent flow and generalized Stokes number evaluated for nominal linear speed of 10 m/s.

<i>Particle size (μm)</i>	<i>Kinetic energy ($\mu\text{J}/\text{particle}$)</i>	<i>Stokes number</i>
774	30.35	4.31
651	18.06	3.40
548	10.77	2.68
450	5.96	2.03
276	1.38	1.02

Each exposure had a duration of 60 min, which was selected to generate measurable weight loss without particle attrition and to avoid overlapping particle imprints on the copper target. Nitrogen purging was not needed since no presence of corrosion was found in a preliminary test run without the erodent particles (see Figure 29, Appendix C). In order to ensure reproducible test conditions for each exposure, a new sample and freshly prepared slurry were used. Each experimental run was repeated producing three replicate samples for weight loss measurement and further analysis. Immediately after each exposure, the sample was rinsed and sonicated, first in distilled water and then in acetone, dried by blowing hot air and then weighed to determine the weight loss.

4.5 Surface analysis method

Each worn surface was subject to analysis by digital image acquisition, followed by processing and finally analysis.

4.5.1 Digital image acquisition

The topography of the worn surfaces was analysed on the curved surface of the samples by a non-contact 3D profilometry technique (Taylor CCI Lite, Taylor Hobson Ltd, Leicester, England). Coherence Correlation Interferometry is an algorithm used to find the coherence peak and phase position of an interference pattern so that the 3D profile may be acquired with high precision. The surface data were recorded with a resolution of 1024×1024 pixels with a field of view of $825 \times 825 \mu\text{m}$ and a real space resolution of $0.825 \mu\text{m}$, and stored in a SURF file format which facilitates software processing prior to the generation of a more convenient display format.

In addition, the morphology of the wear scars was analysed using the secondary electrons (SE) signal of the scanning electron microscope technique (SEM, Hitachi SU-70, Hitachi High-Tech Co, Japan). The SE was used to detect topographic contrast between areas with different depths. The images were recorded with a resolution of 1280×960 pixels, 256 dpi, 8-bit grayscale, and stored in a JPG file format.

4.5.2 Digital image processing

Each 3D profile was handled by the software TalyMap Platinum v. 6.2.7487 (Taylor Hobson Ltd, Leicester, England). First, the surface was levelled by subtraction of a surface found by the least square method. Second, the curved surface shape was removed by a polynomial of the sixth order. Third, non-measured points (<0.05% of data) were filled considering a smooth shape calculated from neighbouring points. Finally, the 3D profile was exported in a grayscale JPG file format, recording the z-scale values.

Each exported image was handled using open-source language programming software – Python 3.7.4 with Numpy, Matplotlib, CV2, and Skimage libraries. First, the local contrast of the image was enhanced by an adjust sigmoid function (Braun, 1999). Second, canny edge detection with a standard deviation of a Gaussian filter of about 3 was used to find the pixels within an area of high local gradients (Niu, Yang, Wang, & Chen, 2011). Third, dilation with a kernel of 3×3 was used to connect close points (“Morphological Image Analysis: Principles and Applications,” 2000). Fourth, an algorithm to find contours proposed by Suzuki was implemented (Suzuki & be, 1985), getting the region of interest (ROI) boxed, i.e. identified wear scars. To avoid the detection of very small objects (debris, local plastic deformation, scratches), a threshold of minimum wear scar size of 9×9 pixels was implemented. Finally, every ROI was exported to a folder for further analysis. The sequence is summarized in Figure 10. The benefit of using this method is the automatic detection of wear scars which reduces the time of selection.

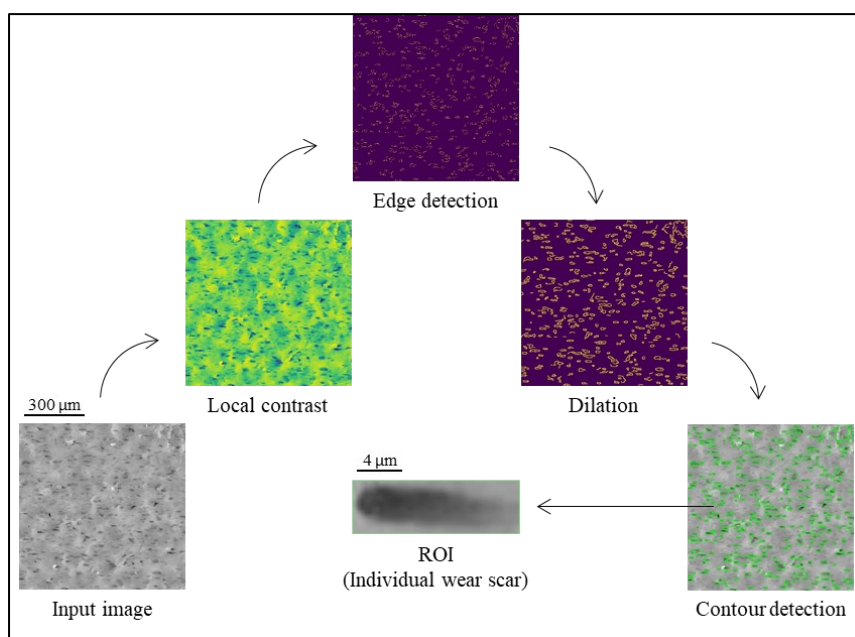


Figure 10. Schematic sequence of the image processing procedure to select data of individual scars from the collective profilometry data.

4.5.3 Digital image analysis

The impact direction (δ) and impact angle (α) were determined considering a moving system of spherical coordinates on the curved target surface (hereafter referred to as global coordinates), as is depicted in Figure 11. The experimental impact direction (δ) was described as the wear scar orientation (ellipse's major axis) on the target surface, which is the projection of the velocity vector YZ on the Y direction. The experimental impact angle (α) was described as the slope of impingement along the impact direction in the wear scar depth profile, which is the projection of the velocity vector XYZ on the YZ plane.

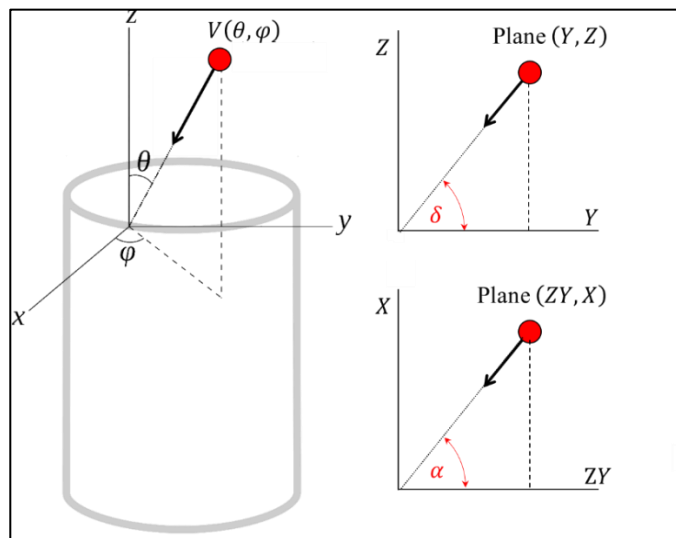


Figure 11. Geometrical description of global coordinates of inclination (θ) and azimuth (φ) angles, and the local coordinates of the direction of impact (δ) and impact angle (α).

Each exported ROI image was handled using Python with the previously described libraries. First, the centroid and the eigenvectors of the ROI were computed, so that the impact direction (δ) was calculated as the deviation of the direction of the principal axis

from the Y direction. Then, the depth profile was extracted along the impact direction, so that the impact angle (α) was calculated from the right slope (impingement direction) (Hao, Dong, Du, Li, & Dou, 2019) regardless of particle or crater size. The indentation depth (h) was calculated as the distance between the minimum point and the average maximum point of the depth profile. A schematic description of the aforementioned definitions is summarized in Figure 12.

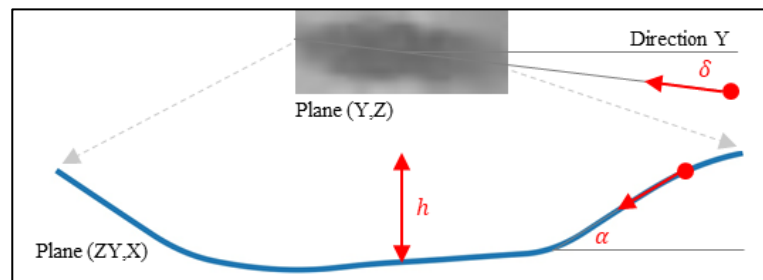


Figure 12. Example of experimental determination of impact angle (α) along the impact direction (δ) for a single particle impact.

The volume wear (E_V) was calculated integrating numerically the volume of the wear scar by the trapezoidal rule, i.e., each slice area along the impact direction is multiplied by the lateral sample resolution of $0.8 \mu\text{m}$. The out of plane plastic deformation, such as ploughing, cutting, or debris in the ROI is subtracted. In Figure 13 it is shown a representative example of a 3D profilometry wear scar.

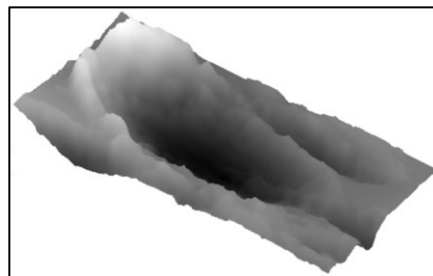


Figure 13. 3D profilometry example of a wear scar produced after erosive exposure.

Finally, by gathering the data of each exported wear scar, a distribution was generated for each measured variable (α , h , E_V). The distribution is displayed in the format of a raincloud plot, which is an approach of data visualization providing maximal statistical information while preserving inference at a glance feature (Allen, Poggiali, Whitaker, Marshall, & Kievit, 2019). The raincloud plot is interpreted as follows:

- The “cloud” is a non-parametric probability density function (kernel density estimate), also known as half-violin-plot, which is helpful for researchers that are used to interpreting histograms.
- The “umbrella” is the standard visualization of central tendency and quartiles below the cloud, also known as the boxplot (Chambers, Cleveland, Kleiner, & Tukey, 2018). The interquartile range (IQR) box represents the middle 50% of the data, i.e., the body of the data.
- The “rain” is raw jittered data points below the cloud, also known as strip-plot. Outliers, observations that lie at an unusual distance from the central values of the data, are visualized as individual points after the fences or whiskers using the Tukey definition (Chambers et al., 2018).

For every particle size range, the boxplot in this work has been built from 300 wear scars from an equivalent region of 2.475 mm \times 2.475 mm. Additionally, if there is any calculation that lies at an unusual distance from the central values of the data (up to 2% of the data in the data set), the observation is inspected and/or removed to assure the absence of meaningless outliers through the Generalized Extreme Studentized Deviate (Generalized ESD) test methodology (Rosner, 1983).

4.6 Global coordinates and kinetic energy

The novelty of the experimental determination of the local coordinates (particle impact direction and impact angle) is that the global coordinates can be retrieved, i.e. approximately the initial conditions that promoted the wear scar imprint on the curved

surface. The velocity vector is described under spherical coordinates on the curved target surface by Eqs. 10-12:

$$V_X = \|V_{XYZ}\| \sin(\theta) \cos(\varphi), \quad (10)$$

$$V_Y = \|V_{XYZ}\| \sin(\theta) \sin(\varphi), \quad (11)$$

$$V_Z = \|V_{XYZ}\| \cos(\theta). \quad (12)$$

Then, using the properties of the dot product, the theoretical impact direction (δ) and impact angle (α) are determined by Eqs. 13 and 14:

$$\cos(\delta) = \frac{V_{YZ} \cdot V_Y}{\|V_{YZ}\| \|V_Y\|} = \frac{\sin(\theta) \sin(\varphi)}{\sqrt{\sin^2(\theta) \sin^2(\varphi) + \cos^2(\theta)}} \quad (13)$$

$$\cos(\alpha) = \frac{V_{XYZ} \cdot V_{YZ}}{\|V_{XYZ}\| \|V_{YZ}\|} = \sqrt{\sin^2(\theta) \sin^2(\varphi) + \cos^2(\theta)} \quad (14)$$

The non-linear system of Eqs. 13 and 14 could be analytically solved if $\alpha \in [0^\circ, 90^\circ]$ and $\delta \in [-90^\circ, 90^\circ]$, determining the inclination angle (Eq. 15) and azimuth angle (Eq. 16):

$$\theta = \begin{cases} \arctan\left(\sqrt{\frac{1}{\cos^2(\alpha) \sin^2(\delta)} - 1}\right), & \delta \geq 0 \\ \pi - \arctan\left(\sqrt{\frac{1}{\cos^2(\alpha) \sin^2(\delta)} - 1}\right), & \delta < 0 \end{cases} \quad (15)$$

$$\varphi = \arcsin\left(\sqrt{\frac{\cos^2(\alpha) \cos^2(\delta)}{1 - \cos^2(\alpha) \sin^2(\delta)}}\right). \quad (16)$$

Finally, the particle kinetic energy of impingement E_k can be separated into two components associated with normal and tangential velocities, respectively, according to Eq. 17:

$$E_k = E_{k_{\perp}} + E_{k_{\parallel}} = \frac{m_p V_X^2}{2} + \left(\frac{m_p V_Y^2}{2} + \frac{m_p V_Z^2}{2} \right) = \frac{m_p \|V_{XYZ}\|^2}{2}. \quad (17)$$

Because the values of velocity are not known without further modelling, only the percentage of kinetic energy associated with tangential or normal velocity components can be determined. These normalized normal and normalized tangential kinetic energies of impingement can be defined by Eqs. 18 and 19, respectively:

$$\hat{E}_{k_{\perp}} = \frac{E_{k_{\perp}}}{E_k} = \left(\frac{V_X}{\|V_{XYZ}\|} \right)^2 = \sin^2(\alpha), \quad (18)$$

$$\hat{E}_{k_{\parallel}} = \frac{E_{k_{\parallel}}}{E_k} = \left(\frac{V_Y}{\|V_{XYZ}\|} \right)^2 + \left(\frac{V_Z}{\|V_{XYZ}\|} \right)^2 = \cos^2(\alpha). \quad (19)$$

4.7 Erosion models

In this section are described the models' parameters used for the back-calculated velocity procedure.

4.7.1 Oka model

The suggested constants and exponents in the predictive equation (Eq. 4) for copper and glass bead particles couple were adopted (Oka & Yoshida, 2005), namely $K = 27$, $k_1 = -0.16$, $k_2 = 2.1$, $k_3 = 0.19$, $n_1 = 2.8 \cdot H_w^{0.41}$, $n_2 = 2.6 \cdot H_w^{-1.46}$, $V' = 100$ m/s, and $D' = 200$ μm .

4.7.2 Huang model

In the lack of data for glass bead particles, the suggested constants for copper and silicon carbide (SiC) particles couple were adopted (Huang et al., 2008) in the predictive equation (Eq. 7), namely $C = 5.5 \cdot 10^{-4}$ and $D = 8.7 \cdot 10^{-2}$.

4.7.3 Cheng model

Cu-ETP properties listed in Table 3 are used in Eq. 9.

4.7.4 Solving method procedure

Given the experimental wear conditions, such as wear volume (Oka, Huang), indentation depth (Cheng), and impact angle, each non-linear equation is solved for the impact velocity through Brent's method (Brent, 1974). Then, in order to focus more on the characteristics and trend of the body of the data (IQR), meaningless velocity outliers were removed using the Tukey definition (Chambers et al., 2018) rather than Generalized ESD test methodology.

5. RESULTS

5.1 Individual and collective features

An example of an individual feature of the surface morphology after the exposure is shown in Figure 14. The shape of the wear scar is elongated with observable lips formed along the longitudinal edges. This morphology is characteristic of the damage mechanism referred to as ploughing, which is typically found for shallow impact angles. Furthermore, zooming out of the previous wear scar reveals that the collective features of the impact angles describe random imprints of shallow impingement angles. In this region, the wear scars have a preferential orientation with low deviation from the nominal flow.

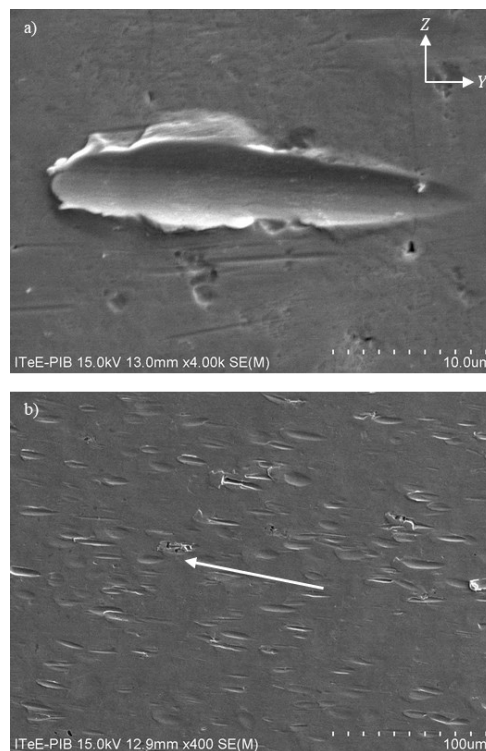


Figure 14. Representative SEM micrographs of: a) individual and b) collective features of wear scars produced by particles of d_p of 276 μm .

5.2 Local coordinates – Impact direction

The distribution of impact direction determined for each particle size is displayed in Figure 15. It is observed that the particle size has no significant effect on the impact direction with respect to location. The overall location of the data set is centred on 0° , i.e. aligned with the tangential flow direction given by the shaft rotation. Furthermore, as the particle size increases, the overall spread (whiskers) weakly decreases; however, this variation between the categories does not display a global tendency because the smallest particle size (276 μm) displays a larger IQR and overall spread than the largest particle size (774 μm).

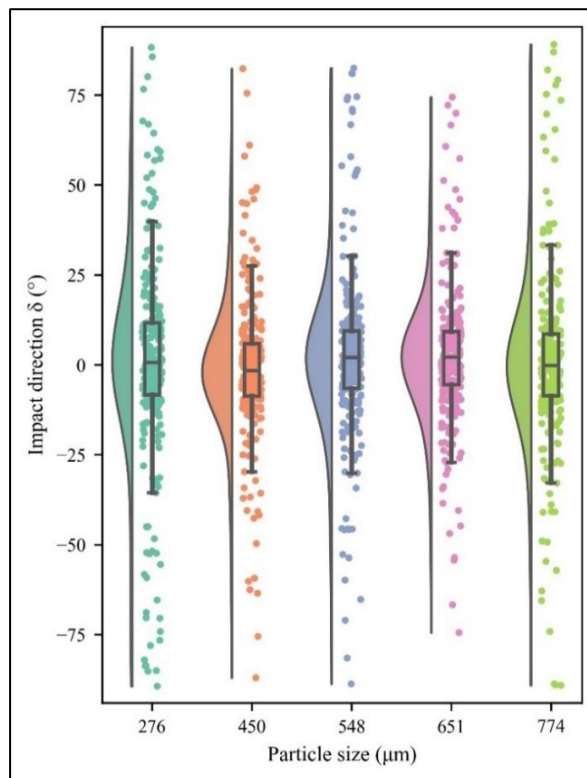


Figure 15. Summary of impact direction distribution determined for each particle size.

Visually, the position of the median in the IQR box and its distance to the whiskers shows that the data set is reasonably symmetric, as seen in the probability density plot. In addition, regardless of the particle size, the outliers show that the particles can reach impact directions at angles as close as $\pm 90^\circ$, although they are not the tendency. No impact direction gap between the data was found.

5.3 Local coordinates – Impact angle

The distribution of impact angle determined for each particle size is displayed in Figure 16. The particle size is found not to have a significant effect on the impact angle with respect to its variation. Each data set is centred at around 7° , i.e. most of the data is associated with shallow impact angles. As the particle size increases, the IQR (50% of the data) and the overall spread (whiskers) do not vary significantly. If the outliers identified by the Tukey definition are not considered, a cut-off impact angle can be established at $\sim 18-19^\circ$ which represents the maximum particle impact angle observed in the experimental set-up as indicated by the upper whiskers in Fig. 16.

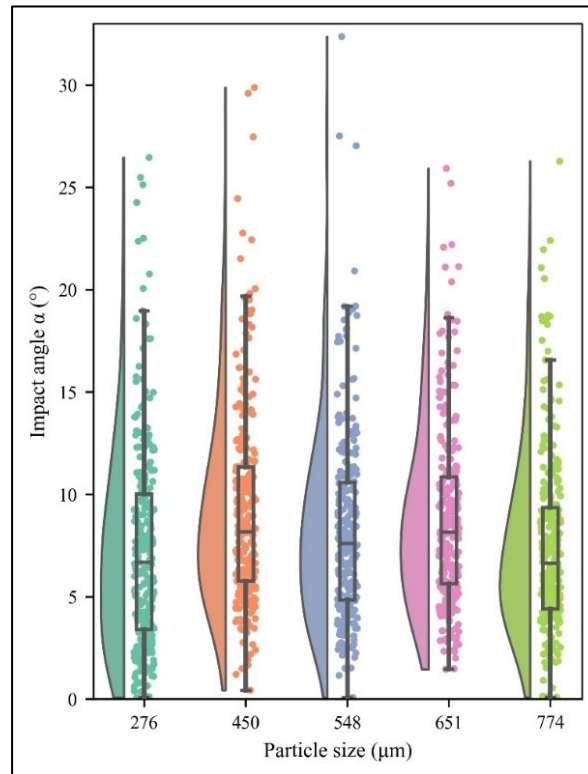


Figure 16. Summary of impact angle distributions determined for each particle size.

Visually, the position of the median in the IQR box and its distance to the whiskers (considering the outliers) shows that the data set is slightly skewed in the positive direction (higher angles), as seen in the probability density plot. In addition, regardless of the particle size, the outliers show that the particles can reach impact angles at least at 30° , although there is no clear tendency. The impact angle gaps found between the data indicate that high impact angles are unusual in this experimental rig.

5.4 Global coordinates – Inclination and azimuth angle

Given the experimental impact direction and impact angle, the previous data could be shown from the point of view of the global coordinates. The inclination angle (θ) and azimuth angle (φ) distribution for each particle size range are displayed in Figure 17.

a)

b)

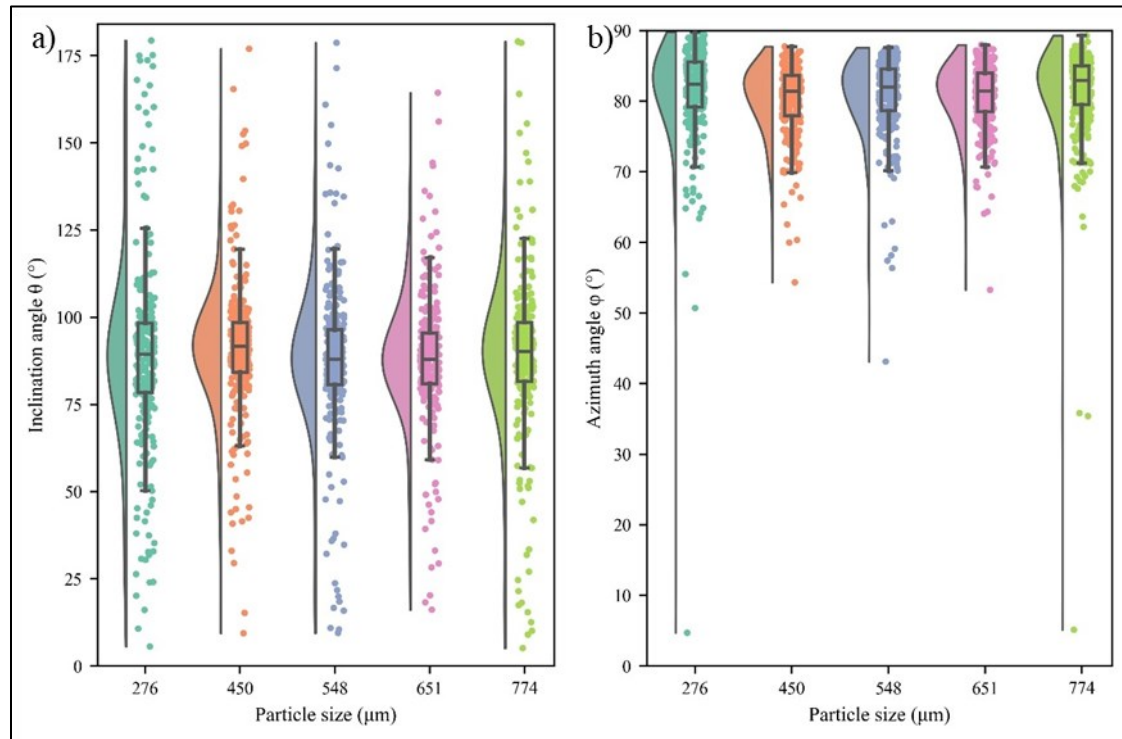


Figure 17. Summary of a) inclination angle (θ) and b) azimuth angle (φ) distributions determined for each particle size.

As shown in Figure 15, the distribution of impact direction spans data between $\pm 90^\circ$; thus, a similar behaviour might be expected to be observed for the inclination angle (Figure 17a). Therefore, the analysis is virtually the same as for the case of impact angle distribution for a given location. Furthermore, in this case, the location of the data set is centred around 90° , i.e. most of the data is centred at a region close to the tangential flow direction given by the shaft rotation.

As shown in Figure 16, most of the impact angles are shallow; thus, a similar tendency can be expected for the azimuth angle (Figure 17b). The analysis is then virtually the same as for the impact angle distribution for a given location. In this case, the location of the data set is centred around 82° , i.e. most of the data is centred at a region close to the tangential flow direction given by the shaft rotation. If the outliers are not considered, a cut-off azimuth angle can be established at $\sim 71^\circ$ as indicated by the lower whiskers in Fig. 17b. The non-linear system of equations (Eqs. 13 and 14) indicates that azimuthal angles

as low as 45° (and even less) might be present; however, the azimuth angle gaps found between the data indicate that low azimuth angles are unusual in this experimental rig.

5.5 Normalized kinetic energy

The normalized normal kinetic energy distribution for each particle size is displayed in Figure 18. Since the two components of the normalized energy sum to 100%, the tangential component is not displayed.

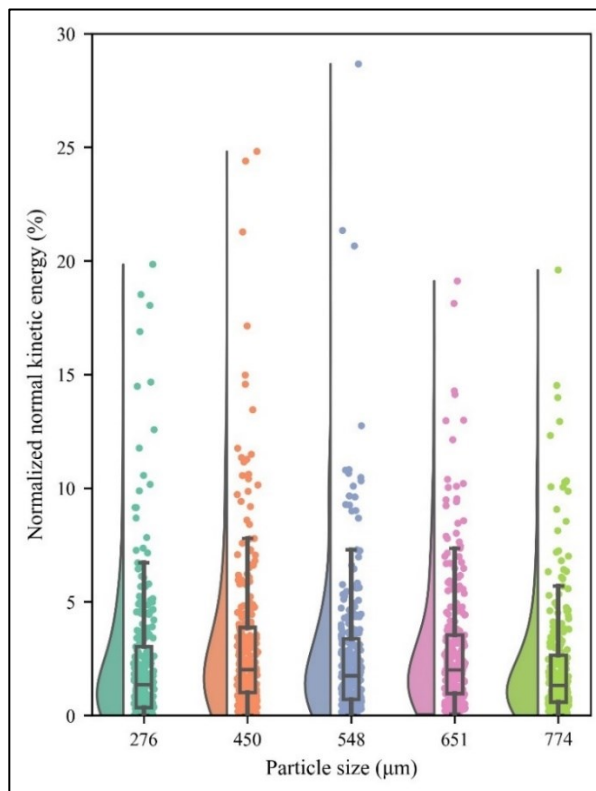


Figure 18. Summary of the normalized normal component of kinetic energy distribution determined for each particle size.

As it was shown in Figure 16, most of the impact angles are shallow; thus, a similar behaviour for the normalized normal kinetic energy can also be expected. It can be seen from a small-angle approximation point of view from the Eq. 18:

$$\sin(\alpha) \approx \alpha \rightarrow \hat{E}_{\perp} = \sin^2(\alpha) \approx \alpha^2 \quad (11)$$

Therefore, the analysis is virtually the same as the impact angle distribution for the given location. Furthermore, the normal energy, which causes the indentation depth imprint and material loss, is centred on 2% of the total impact kinetic energy. If the outliers are not considered, it could be seen that the normal energy could reach up to 20% (and even more); however, the gaps found between the data indicate that these cases are unusual for the experimental rig.

5.6 Wear rate by weight loss

The erosion wear rate determined by weight loss for different particle size ranges is displayed in Figure 19.

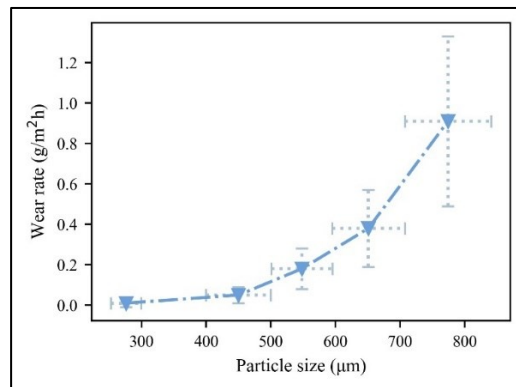


Figure 19. Wear rate determined by weight loss in function of particle size. The dash-dotted line is a visual guide only to connect the triangle markers. The error bars in the particle size correspond to the mesh size. Error bars in the wear rate correspond to experimental statistics.

Figure 19 shows that the particle size has a significant effect on the wear rate. Since the nominal Reynolds number does not vary significantly from the different particle size ranges, it is seen a threshold minimum particle size (or kinetic energy) required to produce measurable weight loss (balance precision 0.1 mg) at 450 μm mean particle size.

5.7 Impact conditions for modelling

The distribution of impact angle, indentation depth, and wear volume determined for each particle size, neglecting meaningless outliers using the Generalized ESD test methodology, is displayed in Fig. 20.

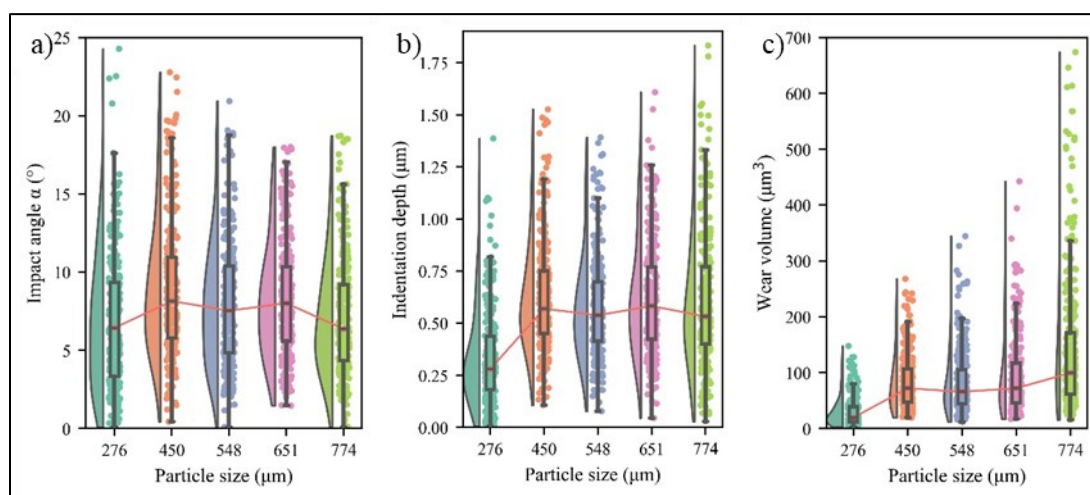


Figure 20. Summary of distributions for different particle sizes: (a) impact angle, (b) indentation depth, and (c) wear volume. Red line connects the median of each distribution.

Impact angle. The results are virtually the same as Fig. 16. The particle size does not show a significant effect on the impact angle with respect to the variation ($\sim 5.26^\circ$ IQR box size) and overall location ($\sim 7.08^\circ$). The location of the data set indicates that most of

the data is centered at shallow impact angles. Furthermore, averaging the upper whisker data for the particle size ranges, it may be established a cut-off impact angle at $\sim 18^\circ$, which roughly represents the maximum particle impact angle observed in the experimental set-up as it is shown in the overall spread of the data, although as the particle size increases the impact angle outliers decrease. Visually, the probability density plot shows that the data set is reasonably positive skewed.

Indentation depth. Particle size does not show a significant effect on the indentation depth with respect to variation ($\sim 0.34 \mu\text{m}$ IQR box size) and overall location ($\sim 0.58 \mu\text{m}$), except for $276 \mu\text{m}$ particle size, which display slightly smaller values, 0.17 and $0.25 \mu\text{m}$ in variation and location, respectively. Besides that, as the particle size increases, the overall spread (see upper whiskers) slightly increases, displaying a global tendency of the data. Visually, the probability density plot shows that the data set is slightly positively skewed.

Wear volume. Particle size shows a significant effect on the wear volume with respect to variation and overall location. For instance, as the particle size increases, the variation increases from 16 to $103 \mu\text{m}^3$ for 276 and $774 \mu\text{m}$ d_p , respectively. The overall location of the data is centered around $83 \mu\text{m}^3$, except for $276 \mu\text{m}$ d_p , which displays a small wear volume ($16 \mu\text{m}^3$). Besides that, as the particle size increases, the overall spread (see upper whiskers) increases, displaying a global tendency of the data. Visually, the probability density plot shows that the data set is reasonably positive skewed.

5.8 Impact velocity

The distribution of impact velocity and kinetic energy determined for each particle size, neglecting meaningless outliers using the Tukey definition, is displayed in Figure 21. The erosion model has a significant effect on the inverse analysis of the impact velocity. While the deconvoluted impact velocity is close to the nominal shaft speed (10 m/s) for Huang and Cheng erosion models, in the case of Oka model it is out of range. Besides that, as the particle size increases, the upper whiskers of the velocity data decreases for every model, and the opposite with kinetic energy, displaying a global tendency of the

data. Visually, the probability density plots show that the data set is reasonably positive skewed.

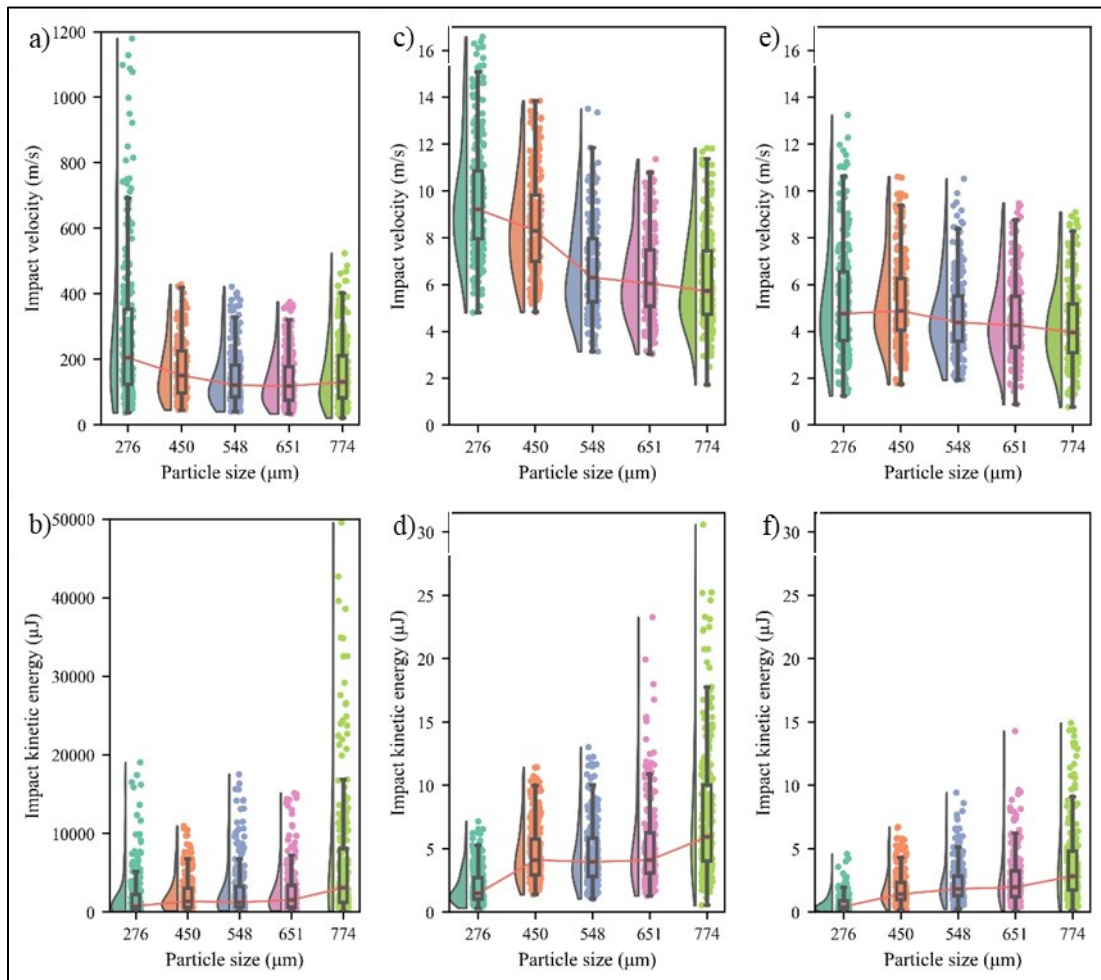


Figure 21. Summary of impact velocity and kinetic energy distribution for different particle sizes: Oka (a,b), Huang (c,d), and Cheng (e,f) erosion models. Red line connects the median of each distribution.

5.9 Wear correlation

The correlation matrix of the experimental variables is displayed in Figure 22 using the Spearman's rank correlation coefficient (Schober & Schwarte, 2018), which is useful when the data sets to be compared do not distribute Gaussian. The correlation between the impact angle and wear volume is weak (0.12), and the correlation between impact angle and indentation depth is moderate (0.69). Statistically, the impact angle is independent of the particle size (0.00). Lastly, as the particle size increases the indentation depth increases (0.24), and jointly with the indentation depth, the wear volume increases as well (0.40, 0.46).

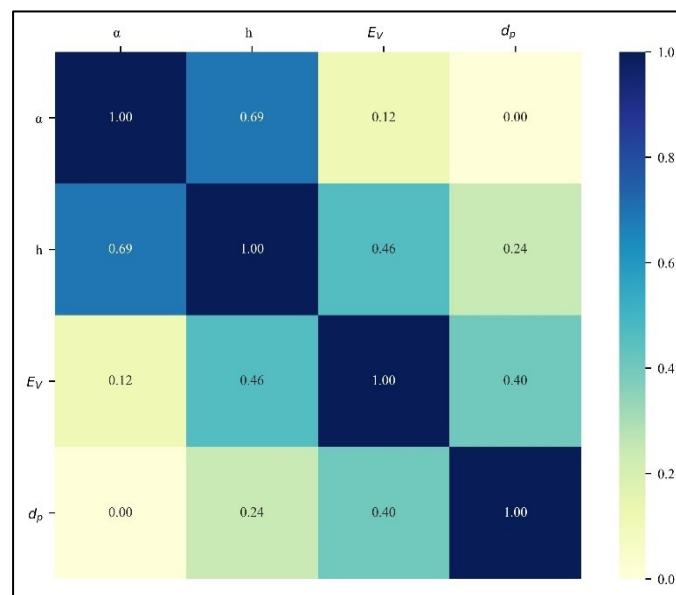


Figure 22. Heatmap of the Spearman correlation matrix for experimental variables.

6. DISCUSSION

6.1 Impact flow conditions

The distributions of impact direction (Figure 15) and inclination angle (Figure 17a) are reasonably symmetrical, which means that sedimentation and gravity do not play a major role in the deviation of the particle from the nominal flow direction set by the rotating surface. This observation is consistent with the high value of Reynolds number. Further, a turbulent boundary layer of the Prandtl-von Kármán log law type is expected in the near-wall region, as it has been observed in the context of a fluid confined in a gap between two rotating cylinders, i.e. Taylor-Couette flow (Grossmann et al., 2016). Then, particles transported tangent to the surface must penetrate this region which involves the transfer of momentum of either eddy flows or turbulent fluctuations. Thus, the misorientation of wear scars must be associated with non-tangential impacts originating from the turbulence raising the question of whether the transfer of momentum from turbulence distributes Gaussian in this experimental rig.

Regarding the distribution of a data set, the Kolmogorov-Smirnov test (KS), which is more sensitive near the centre of the distribution (Karson, 1968), and the Anderson-Darling (AD) test, which is more sensitive to the tails of the distribution (Stephens, 1974), are used to decide if the null hypothesis that the data set comes from a Gaussian distribution could be accepted or rejected.

Table 9 shows the results for the impact direction distribution. At the significance level of 5% ($\alpha = 0.05$), the critical values are about 0.04 and 0.77 for the KS and AD tests, respectively. Since the statistics are significantly higher than the critical values, the null hypothesis is rejected.

Table 9. Statistical tests for verifying the hypothesis of Gaussian distribution. Values determined by Kolmogorov-Smirnov (KS) and Anderson-Darling (AD) tests.

Particle size (μm)	KS statistic	AD statistic	Gaussian hypothesis
774	0.433	6.080	Rejected
651	0.430	11.339	Rejected
548	0.499	16.431	Rejected
450	0.473	13.110	Rejected
276	0.498	5.712	Rejected

Consequently, the data does not comply with a Gaussian distribution (even if potential outliers are neglected by the Generalized Extreme Studentized Deviate Test methodology). In addition to the quantitative analysis, it can be inspected visually with the Gaussian probability plot, previously used for the evaluation of erosive weight distribution (Lindgren & Perolainen, 2014), as it is shown in Fig. 23.

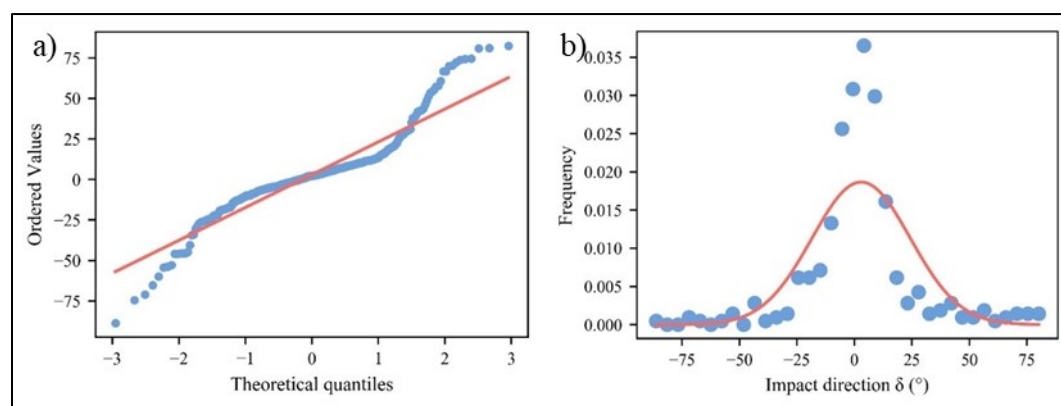


Figure 23. Example of a) Gaussian probability quantile-quantile plot (blue: data, red: Gaussian slope) and b) Point histogram plot (blue: data – bin size of 5°; red: Gaussian fit) for 548 μm d_p .

This result of impact direction distribution not originating from a random near-wall may imply that the turbulent fluctuations themselves may not distribute Gaussian in the transfer of momentum to change the direction of the particles from the nominal tangential direction of flow. Such an effect has been already studied by several authors (Jiménez, 1998; Mouri, Takaoka, Hori, & Kawashima, 2002, 2003; M. Wilczek, Daitche, & Friedrich, 2011; Michael Wilczek, Vlaykov, & Lalescu, 2017), and, in the context of turbulent Taylor-Couette flow, it has been also observed (Teng, Liu, Lu, & Khomami, 2015). For highly turbulent wall-bounded flows, the turbulent fluctuations of the fluid motion behave close to a randomly distributed Gaussian noise far from the walls (bulk or turbulent core). In the case of a slurry pot, this is the gap between the shaft and the container. However, the near-wall statistics show significant deviation from Gaussian noise behaviour, which can be explained by the shear effects of the tangential flow. This interpretation is consistent with our previous finding that, as the Reynolds number increased, the spread of the impact direction distribution evolved from a peak distribution (Dirac distribution) to a symmetrical spread (Molina et al., 2019).

Additionally, a large Stokes number indicates that the particle's trajectory is dominated by its inertia rather than the flow of the medium. Since the Stokes number for the largest particle is four times higher than for the smallest one, it could be expected that the spread of the impact direction should be narrow for the larger particle. However, this is not observed, since this shift on the spread would be more evident when comparing the result of a particle with small Stokes number ($Stk < 0.1$) with the one of a large Stokes number ($Stk > 1$), which is not the case in this study.

On the other hand, the actual impact velocities of particles on an eroding target may differ significantly from the free stream velocity of the suspension due to the energy required to displace the liquid separating an approaching particle from the target surface, i.e. the squeeze film, as pointed out by Clark (H. Mc I. Clark, 1992). In other words, the increase of the drag force in the proximity of the target surface accounts for the energy loss expressed during the deceleration. However, there was evidence of particle impact for every particle size used in this study, indicating that particles of each size possessed enough kinetic energy to penetrate the squeeze film.

It is worthy to mention that an estimation of the impact direction distribution could be fitted with the purpose of further modelling or mechanistic explanation. For example, this could be done by performing the Kolmogorov-Smirnov test for all the families of distributions available in the Scipy library, choosing the best fitting by comparing with the maximum p-value and/or the minimum sum of the squared estimate of error (SSE).

6.2 Particle impact conditions

The distribution of the impact angle (Figure 16) and azimuth angle (Figure 17b) indicates that the turbulent fluctuations that determine the effective impact angle come from the normal axis to the plane (X direction) and incoming random near-wall eddies that succeed penetrating the viscous layer. As the tangential flow is the dominant orientation, it is expected that the distribution may not be symmetrical. In this sense, the data sets could be fit in the same way as explained for the impact direction (Section 6.1); however, in this case, the family of distribution must comply with the definition of a positive domain ($\alpha, \varphi > 0$).

On the other hand, the impact angle and velocity of particles impinging a target surface are known to determine the mechanisms of material removal. Whereas the normal velocity is mostly associated with the wear scar indentation depth, and the tangential velocity mostly explains the shape of the wear scar, as suggested by Bitter (1963). In our case, the major transfer of kinetic energy is given by the tangential component (98%) regardless of the particle size. Therefore, the wear rate data in Figure 19 can mostly be explained by the tangential component of the kinetic energy. This observation may raise the question of whether the experimental set-ups used in slurry erosion, such as pot tester and jet erosion tester (the most used ones (More, Bhatt, & Menghani, 2017)) may have a roughly controlled and evaluated dispersion of particles' impact direction and impact angle on the target surface. For example, in the case of observing that an experimental rig would not show a high probability of normal impacts known to induce fracture or crack propagation in brittle materials, these wear mechanisms could not be studied in that

experimental set-up. The above is our case because most of the impacts are shallow and the energy is transferred tangentially.

Finally, a possible correlation between the experimental impact direction and impact angle, i.e. a degree to which both variables are dependent upon each other, is examined. This could be evaluated by means of the Spearman's rank correlation coefficient (Schober & Schwarte, 2018), which is useful when the data sets to be compared do not distribute Gaussian. The results are summarized in Table 10.

Table 10. Spearman's rank correlation coefficient between impact direction and impact angle at different particle sizes.

<i>Particle size (μm)</i>	<i>Correlation coefficient</i>	<i>Interpretation</i>
774	0.24	Weak
651	0.12	Weak
548	0.09	Negligible
450	0.15	Weak
276	0.17	Weak

The correlation coefficients in Table 10 are all positive but significantly lower than 1, which would be indicative of a perfect monotone correlation. Therefore, neither moderate nor strong correlation was found in the experiment and the two variables can be considered independent of each other, which are also presented visually in Figure 24. This result is relevant for wear studies because it means that no direct or indirect information on the impact angle can be retrieved from 2D images (e.g., SEM) because it only contains information on the impact direction distribution in the *ZY* plane. Consequently, 3D profilometry data is indispensable for acquiring detailed information about the local impact conditions.

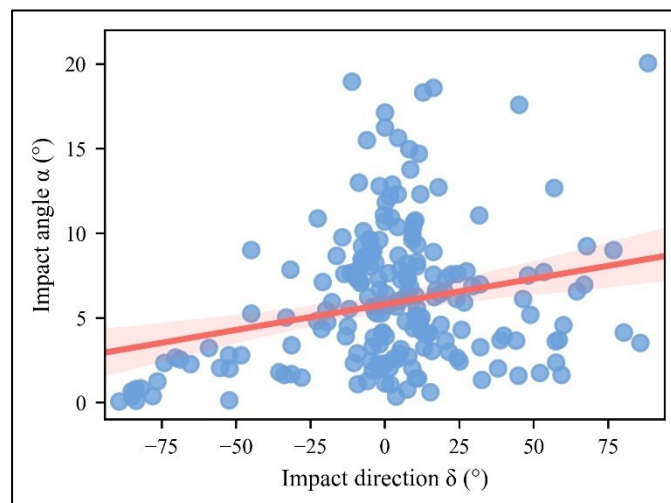


Figure 24. Example of correlation between impact direction and impact angle determined for the particle size of 276 μm .

6.3 Implications for wear analysis

Firstly, both the angle distributions (Figure 16 and 17) and the normalized kinetic energy (Figure 18) reveal that most of the kinetic energy (98%) is transferred by the tangential component of the impact velocity at shallow impact angles ($\alpha \sim 8^\circ$) with a preferential impact direction given by the flow conditions ($\delta \sim 90^\circ$). Consequently, the wear data obtained by weight loss (Figure 19) correspond to specific and identified impact conditions and not the unknown conditions typically associated with this type of erosion pot. Further, the cut-off angle in the range of $\sim 18\text{-}20^\circ$ is in the typical region of the maximum wear rate for ductile materials (which is the case of Cu-ETP used here), which means that, in this slurry pot system, the wear rate is limited to a narrow region of impact angles that can be characterized with confidence.

Secondly, the dominant wear mechanisms expected in this experimental rig are ploughing for spherical particles and cutting for angular particles (see Section 5.1). Considering that at the shallow impact angles, the influence of particle rotation becomes

relevant (Ben-Ami & Levy, 2016; Deng, Bingley, & Bradley, 2004); the effect particle's back-spin and/or top-spin should be taken into account as a possible source of modified wear scar morphology. However, dedicated research is needed to collect the necessary wear scar data, which is beyond the scope of this work.

Lastly, in our experimental set-up, the particle size dependence on the wear rate is about $\sim d_p^5$. The value of the exponent is higher than that reported by other authors (0.2-4.0) (Javaheri et al., 2018). Although this range was found for other configurations of the erosion test, only one being a slurry pot (Desale, Gandhi, & Jain, 2011), our finding shows that the exponent is sensitive to the local impact conditions determined by the experimental rig and procedure. In particular, the wear rate is expected to be proportional to the kinetic energy conveyed by the particles (Bitter, 1963; Hector McI. Clark & Wong, 1995; Finnie, 1960a; Uzi & Levy, 2018), and thus, an explicit relationship of d_p^3 should be expected for spherical particles. Therefore, the parametric factor of $\sim d_p^2$ should be the exclusive addition of our particular experimental rig, because there is no imminent physical meaning to it more than the slurry concentration ($\sim d_p^3$) or particle cross-sectional area (d_p^2). At the current state of the art, however, it is not fully clarified how these factors should be considered in the wear loss account on a theoretical basis. Furthermore, the threshold minimum particle size below which minimal erosion is produced was found to be around 450 μm , but no critical particle diameter was found above which any increment of erosion follows. Both these critical values have been reported and discussed by several authors (Uzi & Levy, 2019). Once again, the particularities of local impact conditions determined by the experimental rig may affect the conclusions on the effect of variables such as particle size.

6.4 Feasibility of the diagnostic tool

The surface topography patterns associated with wear scars were quantified by means of image analysis of 3D profilometry data in terms of the experimental impact direction and impact angle. The curved shape of the samples was successfully removed

by the algorithm implemented in TalyMap Platinum v. 6.2.7487 avoiding typical artefacts (unusual peaks, valleys, elongated/constrained scars, etc.).

The method has been shown to be robust for the identification of individual features (wear scars) even in the presence of highly plastic deformation (lips, ploughing) or debris. The material used in this study, Cu-ETP, is a soft material, for that reason, the first stage of the wear scar imprints is easier to be studied. However, a hard material would show a high degree of fracture and crack propagation in the impact zones (Y. F. Wang & Yang, 2008), which is a further direction of extending the characterization methodology presented here. Another point to consider is the slurry concentration. In the dilute slurry, there is a lesser probability of overlapping of the impingement features; thus, a concentrated slurry would shorten the time needed for steady-state and a higher degree of surface topography distortion would be found (Xie, Clark, & Hawthorne, 1999). For these reasons, an even more difficult and robust algorithm should be defined and implemented.

Notwithstanding, it is worth mentioning that, if the standard deviation of the Gaussian filter (SDGF) in the canny edge detection is decreased, more features are available for the algorithm to be detected. These additional features may correspond to local lips, ploughing, or debris rather than further wear scars. This issue could be dealt with a built-in threshold minimum wear scar size (TMWSS), adjusting this value according to the dimensions of the image (or 3D profilometry data) and user requirements. In summary, two fine-tuning parameters could be set in the algorithm: SDGF and TMWSS. The effect is illustrated in Figure 25.

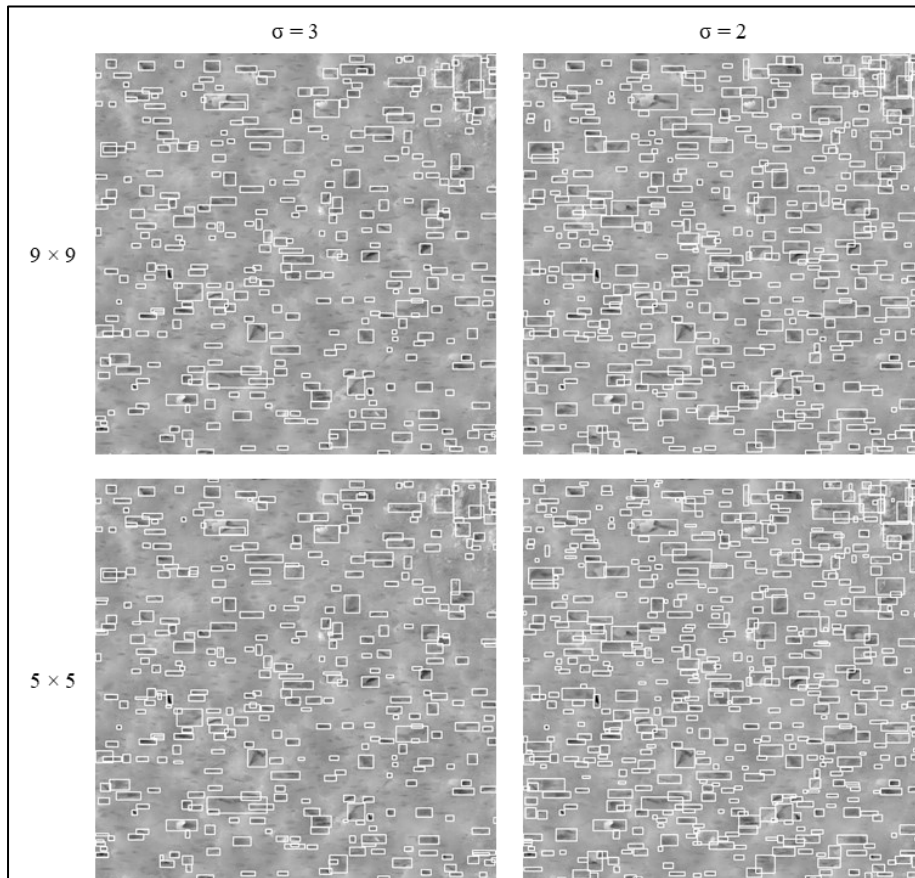


Figure 25. Wear scar detection of scar pattern produced by the particle size of 774 μm . White boxes enclose the identified wear scars. Detected features are shown in a matrix of four combinations of threshold parameters: SDFG ($\sigma = 3$ or 2) and TMWSS (9×9 or 5×5).

Further improvements to the algorithm might consider removing detected wear scars that display positive depth indentation and/or negative volume, i.e. features that are out of the deformation plane. Also, the data of individual wear scars extracted with the implemented image processing might be used as an input library for alternative implementations of wear scar recognition using artificial intelligence, similar to that proposed by Peng and Wang (Peng & Wang, 2019) for the recognition of wear particles using a convolutional neural network (CNN) algorithm. In conclusion, there are various

opportunities for improving the method proposed here for extracting information on erosive wear.

6.5 Dimensions of individual erosion wear scars

The impact angle distributions (Figure 20a) disclose that most of the impacts are shallow ($<25^\circ$) regardless of the particle size. It means that most of the particle kinetic energy shown in Figure 21 is transferred by the tangential component of the impact velocity depicted in a friction force, which responsible for the shape of the wear scar rather than its indentation depth. Consequently, the indentation depth distributions (Figure 20b) are expected to display very small imprints ($h/d_p < 0.3$), facing the challenge of an appropriate calculation of the wear volume. For instance, for the collision of the smaller particle size (276 μm), the median of the height and wear volume is 0.25 μm and 16 μm^3 , respectively. Considering the glass bead as a perfect sphere, the crater size, which geometrically corresponds to the base of the spherical cap or dome, would be ~ 12 μm without considering the crater length that should be higher than 12 μm due to the shallow impact angles found. Then, being the lateral sampling resolution of 0.8 μm , in this zone, there are 15x15 profilometry measurements. Thus, these wear scars imprints are possible to acquire despite the small ratio indentation depth and particle size.

Although the particle size has no significant effect on the location of the impact angle and indentation depth (except for 276 μm), the impact kinetic energy does depend strongly on the particle size due to its mass dependence. Additionally, as the particle size increases, also the chances of a bigger crater size. This would explain why the wear volume distribution (Figure 20c) displays a global tendency with respect to variation and overall spread as the particle size varies, which is not seen in the impact angle and indentation depth. However, the interpretation could differ according to how the data is displayed in wear, as it has been pointed out in the literature (Valtonen, Ojala, Haiko, & Kuokkala, 2019). For instance, it is common in the literature the normalization by particle mass of the results, which is no other thing that normalization by d_p^3 . In Fig. 26b it could be seen that 1 kg of erodent could produce the same wear damage in the range 276–450

and 548–651 μm , which indicates that kinetic energy would play an undefined role. In addition, Fig. 26a shows a nonsense scenario because the normalization is not suitable for the slurry pot system. Thus, the normalization could play a role, but it should be done carefully.

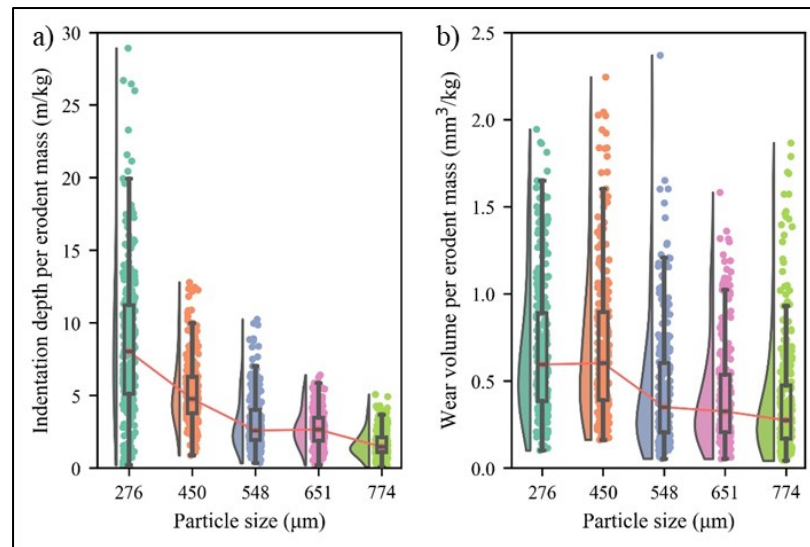


Figure 26. Wear damage normalized by erodent mass: (a) Indentation depth, (b) Wear volume.

6.6 Erosion models

The inverse analysis of the impact velocity for each wear scar was done by means of three models: Oka, Huang, and Cheng.

Regarding the wear variable used for the inverse analysis of the impact velocity, even though Huang and Cheng models rely on the measurement of the wear volume and indentation depth, respectively, which are very small for a single wear scar at 276 μm d_p , small measured values did not affect the inverse analysis with meaningless results. However, Oka model resulted in nonsense impact velocities (Figure 20), and even though this model has reported the best overall predictive performance in several configurations

(Messa et al., 2019; Pereira et al., 2014; Zheng et al., 2019), if the purpose is to deconvolute the local impact velocity of a single imprint, this model fails by overestimating the result. This drawback may be explained by the reference speed of 100 m/s used to set up the experimental constants, which may be too far from the nominal shaft speed of 10 m/s used in this experiment.

On the other hand, Huang model coefficients have been retrieved from experiments which involve collective and successive particle impacts on the target surface, therefore, it includes mechanisms such as the removal of plastic damage in the surroundings of the wear scars (plastic deformation out of plane, due to ploughing or cutting) or shield effect by particle-particle interactions (Messa & Malavasi, 2018) that are not considered in a single impact model. Conversely, Cheng model is derived from a theoretical formulation of a single impact, which does not consider the aforementioned phenomena. Besides that, being Huang an empirical formulation and Cheng a theoretical one, both have surprisingly very similar results and trends, and they are closer to the nominal shaft speed than Oka model; even though Huang coefficients have been calculated for SiC particles and not glass beads. It should be kept in mind that this result holds for dilute slurry, where no particle-particle interaction is present, which is especially important for Cheng model.

Regarding the range of the velocity distributions, it might be explained by the turbulent fluctuations in the context of a fluid confined in the gap between two rotating cylinders, i.e., Taylor-Couette flow. Measurements in the turbulent regime display fluctuations up to ~4% of the shaft speed (Grossmann, Lohse, & Sun, 2014). If this is the case, flow velocity close to the wall should be in the range of 9.6 – 10.4 m/s, but if the relative particle velocity at the moment of impact should be less than the nominal linear velocity, the three models are depicting values above this range. Additionally, another explanation of this bigger spread of the data could be related to the four baffles mounted at 90° and the pivot bearing at the bottom of the slurry container. However, once again, turbulent fluctuations up to 100%, which is seen for Huang and Cheng models (i.e. 20 m/s) are physically unfeasible, although Cheng displays most of its data in the possible range in comparison to Huang.

Lastly, impact kinetic energy derived from Oka and Huang models show a constant trend (median, IQR, upper whiskers) in the range of 450–651 $\mu\text{m } d_p$, which is the same that happens with the wear volume distributions that these models used. On the other hand, Cheng model displays a positive trend in this range as the particle size increases, which does not take place with the indentation depth distribution, being less clear the trend in this range, especially for 548 $\mu\text{m } d_p$. Thus, it is not clear from the data if the impact energy in this range remained the same in the real conditions because the interpretation of its estimation would depend on the variable used for the inverse analysis. Nevertheless, the global tendency would point to positive a positive trend, having Cheng the best outcome on this issue.

Thus, the above results suggest that the theoretical elastic-plastic model of Cheng provides a better fitting than empirical models for the deconvolution of the statistical impact conditions without involving experimental coefficients. Moreover, one of the strengths of the theoretical models is that the mechanical properties of the target material required as input, such as its density, yield strength, and Young's modulus, are generally known. Much effort is required to deepen into the physical mechanisms of particle flow and impact erosion in order to increase the reliability of the models, especially the empirical ones.

In the meantime, this work shows that central tendency values (median or mean) of the theoretical model are representative of the impact conditions, however, values far from the central tendency should be considered carefully if not avoided for an inverse analysis interpretation of an eroded sample. Moreover, combining the particle velocity with the impact angle (and directionality, Fig. 15), the three spatial components of the velocity vector could be retrieved, recreating each particle collision with the target surface without prior information.

6.7 Wear correlation: Feasibility of the inverse analysis

If any inverse analysis is to be done for individual wear scars, the assumptions of the models should be tested. Since several authors have published the dependence of wear

and impact angle from experiments that involved collective and successive impacts (Javaheri et al., 2018), it may be interesting to figure out if the correlation still holds for the case of individual wear scars (Fig. 14).

First of all, according to Fig. 22, the correlation between impact angle and wear volume is weak, which means that these variables do not display any nonlinear monotonic trend as it has been reported in the literature (typically a sine, cosine, or polynomial correlation) (Javaheri et al., 2018). Surprisingly, the Huang model, which depends on the nonlinear trend assumption (sine-cosine correlation, see equation (4)), manages to get very good results despite the absence of an experimental trend. Nevertheless, the bigger correlation between impact angle and indentation depth would support the use of the Cheng model.

Thus, to elaborate more on the relationship between the impact angle and wear volume, in Figure 27 it is shown the widespread normalization by particle mass and impact kinetic energy:

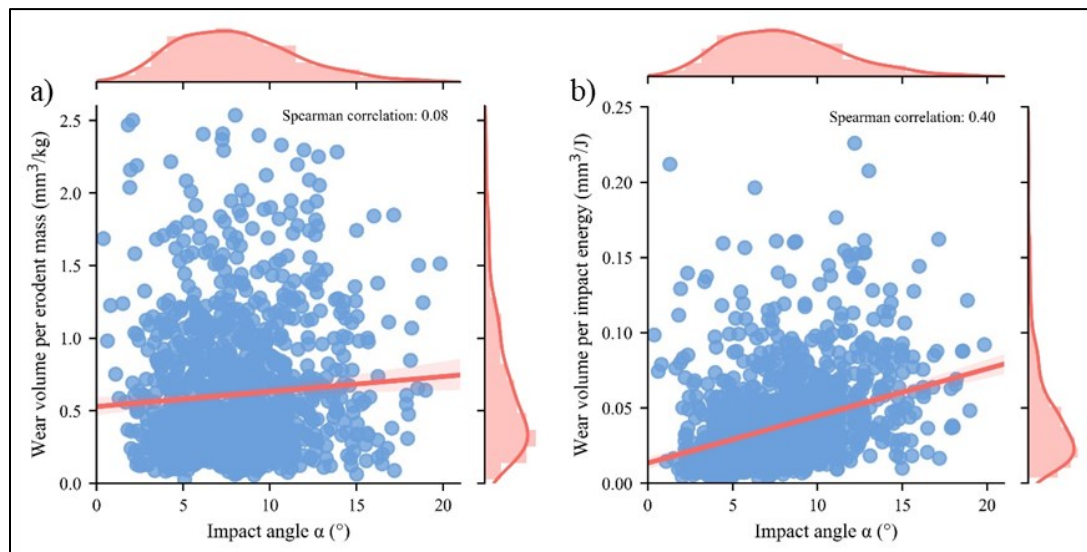


Figure 27. Scatter plot of wear volume per: a) erodent mass and b) impact kinetic energy of erodent (estimated from Cheng model, Fig. 6). Linear regression only was shown to visually guide the correlation between the variables.

As it is seen in Figure 27, the correlation between impact angle and wear volume per unit of erodent mass is negligible (0.08), although this correlation has been reported as strong in previous works from collective and successive impacts (Javaheri et al., 2018). This difference might not be related to the impact velocity, since this relationship has been investigated in a wide range of velocities, 14–104 m/s, according to the data gathered by Uzi and Levy (2018). Moreover, some facts should be kept in mind: in this case, the erosion rate and impact angle are calculated for each wear scar, but in other studies, the erosion rate is measured as a whole, i.e., the weight loss of the sample after the test, and the impact angle is fixed beforehand. To the best of our knowledge, this is the first experimental study that addresses the individual account for the elaboration on the impact angle dependence, particularly at angles less than 10° . Thus, much collaborative effort is required to delve deeper into this.

On the other hand, the correlation between impact angle and wear volume per impact kinetic energy is moderate (0.40), which indicates that this is a better indicator of the wear rate curve from the individual impact point of view. This result is aligned to the work of Bitter or Finnie (Finnie, 1960b), i.e., when the ‘deformation’ erosion is neglected at small angles, the ‘cutting’ erosion is described by a monotone relationship (sine-cosine) of the wear volume per impact energy and the impact angle. Although this correlation coefficient might vary if the particle size distribution is considered, the change should be slightly due to the narrow mesh range used in this study.

7. CONCLUSIONS

The image processing procedure employed to 3D profilometry data of wear scars produced on copper in highly turbulent dilute slurry is concluded to be applicable for meaningful identification of the global flow conditions and the local particle impact conditions, both deduced from the worn surfaces. In particular, it is found that the statistical distribution of impact direction is not Gaussian, which is explained by the shear effects on the near-wall turbulent fluctuation. The distribution of impact angle is found positively skewed towards shallow impingements and most of the kinetic energy conveyed per particle was found dissipated in the tangential direction, which is associated with ploughing as the mechanism of material removal, with a particle size dependence of the wear rate of about $\sim d_p^5$.

This preliminary work provides a potential tool for the understanding of the erosion damage by means of an inverse analysis of worn surfaces. The information about the flow regime and impact conditions can be deduced with no prior knowledge of the erosive flow set-up. In fact, the inverse analysis procedure employed to 3D profilometry data is concluded to be applicable for meaningful identification of central tendency values of the collective impact conditions.

Both experimental and theoretical models can retrieve reasonable particle impact velocities; however, the predictions of empirical models developed for other set-ups may result in discrepancy, as it is the case of Oka (overestimated) and Huang (closer to nominal conditions). The simple theoretical elastic-plastic model of Cheng provided the closest results to the nominal flow conditions. Thus, this work provides an inverse analysis framework for the determination of the particle impact conditions on erosion damage. Combining experimental observations with modeling of individual impacts allows extracting complete information of the three spatial components of the velocity vector of each particle colliding the target surface. Notwithstanding, further work into the role of the experimental and theoretical models in the inverse analysis of the impact velocity is necessary for generalizing these findings.

Further, unlike the previous work in collective and successive impacts, the correlation between wear volume and impact angle could not have been shown in the statistical analysis of individual features, not even when normalizing per erodent mass. However, the wear volume per impact kinetic energy does show a non-negligible correlation with the impact angle.

Lastly, from the discussion conducted in this research it follows that for drawing further conclusions on the impact conditions for individual and collective features, future work should be focused on robust image detection and complementary experiments. Moreover, computational fluid dynamics of the test runs can be contrasted with the data shown in this work. Likewise, numerical analysis of the deformation may show the energy scale and wear scar shape for each impact. Thus, the extended analysis is necessary to verify the robustness of the method to bridge the scales of local impact conditions in a turbulent flow with the global erosive wear.

REFERENCES

- Abd-Elrahman, Y. M., Abouel-Kasem, A., Ahmed, S. M., & Emara, K. M. (2014). Stepwise Erosion as a Method for Investigating the Wear Mechanisms at Different Impact Angles in Slurry Erosion. *Journal of Tribology*, 136(2), 021608. <https://doi.org/10.1115/1.4026420>
- Abd-Elrhman, Y. M., Abouel-Kasem, A., Ahmed, S. M., & Emara, K. M. (2014). Stepwise Erosion as a Method for Investigating the Wear Mechanisms at Different Impact Angles in Slurry Erosion. *Journal of Tribology*, 136(2), 021608. <https://doi.org/10.1115/1.4026420>
- Abouel-Kasem, A. (2011). Particle size effects on slurry erosion of 5117 steels. *Journal of Tribology*. <https://doi.org/10.1115/1.4002605>
- Al-Bukhaiti, M. A., Ahmed, S. M., Badran, F. M. F., & Emara, K. M. (2007). Effect of impingement angle on slurry erosion behaviour and mechanisms of 1017 steel and high-chromium white cast iron. *Wear*. <https://doi.org/10.1016/j.wear.2006.11.018>
- Alam, T., Aminul Islam, M., & Farhat, Z. N. (2015). Slurry Erosion of Pipeline Steel: Effect of Velocity and Microstructure. *Journal of Tribology*, 138(2), 021604. <https://doi.org/10.1115/1.4031599>
- Alam, T., & Farhat, Z. N. (2018). Slurry erosion surface damage under normal impact for pipeline steels. *Engineering Failure Analysis*, 90(December 2016), 116–128. <https://doi.org/10.1016/j.engfailanal.2018.03.019>
- Allen, M., Poggiali, D., Whitaker, K., Marshall, T. R., & Kievit, R. A. (2019). Raincloud plots: A multi-platform tool for robust data visualization [version 1; peer review: 2 approved]. *Wellcome Open Research*, 4, 1–41. <https://doi.org/10.12688/wellcomeopenres.15191.1>
- Andrews, N., Giourntas, L., Galloway, A. M., & Pearson, A. (2014). Effect of impact angle on the slurry erosion-corrosion of Stellite 6 and SS316. *Wear*, 320(1), 143–151. <https://doi.org/10.1016/j.wear.2014.08.006>
- Ayres, C., Bowlin, G. L., Henderson, S. C., Taylor, L., Shultz, J., Alexander, J., ... Simpson, D. G. (2006). Modulation of anisotropy in electrospun tissue-engineering

- scaffolds: Analysis of fiber alignment by the fast Fourier transform. *Biomaterials*, 27(32), 5524–5534. <https://doi.org/10.1016/j.biomaterials.2006.06.014>
- Ayres, C. E., Bowlin, G. L., Pizinger, R., Taylor, L. T., Keen, C. A., & Simpson, D. G. (2007). Incremental changes in anisotropy induce incremental changes in the material properties of electrospun scaffolds. *Acta Biomaterialia*, 3(5), 651–661. <https://doi.org/10.1016/j.actbio.2007.02.010>
- Ayres, C. E., Jha, B. S., Meredith, H., Bowman, J. R., Bowlin, G. L., Henderson, S. C., & Simpson, D. G. (2008). Measuring fiber alignment in electrospun scaffolds: A user's guide to the 2D fast Fourier transform approach. *Journal of Biomaterials Science, Polymer Edition*, 19(5), 603–621. <https://doi.org/10.1163/156856208784089643>
- Ben-Ami, Y., & Levy, A. (2016). Absorbed shear energy during solid particle impact on ductile surface. *Wear*, 368–369, 162–172. <https://doi.org/10.1016/j.wear.2016.09.021>
- Biswas, S., Williams, K., & Jones, M. (2018). Development of a constitutive model for erosion based on dissipated particle energy to predict the wear rate of ductile metals. *Wear*, 404–405(March), 166–175. <https://doi.org/10.1016/j.wear.2018.02.021>
- Bitter, J. G. A. (1963). A study of erosion phenomena. Part II. *Wear*, 6(3), 169–190. [https://doi.org/10.1016/0043-1648\(63\)90073-5](https://doi.org/10.1016/0043-1648(63)90073-5)
- Brake, M. R. W. (2015). An analytical elastic plastic contact model with strain hardening and frictional effects for normal and oblique impacts. *International Journal of Solids and Structures*, 62, 104–123. <https://doi.org/10.1016/j.ijsolstr.2015.02.018>
- Braun, G. J. (1999). Image lightness rescaling using sigmoidal contrast enhancement functions. *Journal of Electronic Imaging*. <https://doi.org/10.1117/1.482706>
- Brent, R. P. (1974). Algorithms for Minimization Without Derivatives. *IEEE Transactions on Automatic Control*. <https://doi.org/10.1109/TAC.1974.1100629>
- Burson-Thomas, C. B., & Wood, R. J. K. (2017). Developments in Erosion–Corrosion Over the Past 10 Years. *Journal of Bio- and Tribo-Corrosion*, 3(2). <https://doi.org/10.1007/s40735-017-0073-4>
- Cao, W., Zhang, H., Wang, N., Wang, H. W., & Peng, Z. X. (2019). The gearbox wears state monitoring and evaluation based on on-line wear debris features. *Wear*, 426–427(December 2018), 1719–1728. <https://doi.org/10.1016/j.wear.2018.12.068>

- Chambers, J. M., Cleveland, W. S., Kleiner, B., & Tukey, P. A. (2018). Graphical methods for data analysis. In *Graphical Methods for Data Analysis*. <https://doi.org/10.1201/9781351072304>
- Cheng, J., Zhang, N., Wei, L., Mi, H., & Dou, Y. (2019). A new phenomenological model for single particle erosion of plastic materials. *Materials*, 12(1). <https://doi.org/10.3390/ma12010135>
- Clark, H. M., & Llewellyn, R. J. (2001). Assessment of the erosion resistance of steels used for slurry handling and transport in mineral processing applications. *Wear*, 250–251(PART 1), 32–44. [https://doi.org/10.1016/S0043-1648\(01\)00628-7](https://doi.org/10.1016/S0043-1648(01)00628-7)
- Clark, H. Mc I. (1992). The influence of the flow field in slurry erosion. *Wear*, 152(9–10), 223–240. [https://doi.org/10.1016/0043-1648\(92\)90122-O](https://doi.org/10.1016/0043-1648(92)90122-O)
- Clark, H. Mc I., & Hartwich, R. B. (2001a). A re-examination of the “particle size effect” in slurry erosion. *Wear*, 248(1–2), 147–161. [https://doi.org/10.1016/S0043-1648\(00\)00556-1](https://doi.org/10.1016/S0043-1648(00)00556-1)
- Clark, H. Mc I., & Hartwich, R. B. (2001b). A re-examination of the “particle size effect” in slurry erosion. *Wear*. [https://doi.org/10.1016/S0043-1648\(00\)00556-1](https://doi.org/10.1016/S0043-1648(00)00556-1)
- Clark, H. McI. (2002). Particle velocity and size effects in laboratory slurry erosion measurements OR... do you know what your particles are doing? *Tribology International*, 35(10), 617–624. [https://doi.org/10.1016/S0301-679X\(02\)00052-X](https://doi.org/10.1016/S0301-679X(02)00052-X)
- Clark, Hector Mc I. (1991). On the impact rate and impact energy of particles in a slurry pot erosion tester. *Wear*, 147(1), 165–183. [https://doi.org/10.1016/0043-1648\(91\)90127-G](https://doi.org/10.1016/0043-1648(91)90127-G)
- Clark, Hector McI., & Wong, K. K. (1995). Impact angle, particle energy and mass loss in erosion by dilute slurries. *Wear*, 186–187, 454–464. [https://doi.org/10.1016/0043-1648\(95\)07120-2](https://doi.org/10.1016/0043-1648(95)07120-2)
- D.N. Veritas. (2011). Recommended Practice, DNV RP-O501, Erosive Wear in Piping Systems. 10.
- Deng, T., Bingley, M. S., & Bradley, M. S. A. (2004). The influence of particle rotation on the solid particle erosion rate of metals. *Wear*, 256(11–12), 1037–1049. [https://doi.org/10.1016/S0043-1648\(03\)00536-2](https://doi.org/10.1016/S0043-1648(03)00536-2)

- Desale, G. R., Gandhi, B. K., & Jain, S. C. (2011). Development of Correlations for Predicting the Slurry Erosion of Ductile Materials. *Journal of Tribology*. <https://doi.org/10.1115/1.4004342>
- Finnie, I. (1960a). Erosion of surfaces. *Wear*, 3, 87–103.
- Finnie, I. (1960b). Erosion of surfaces by solid particles. *Wear*, 3, 87–103.
- Frosell, T., Fripp, M., & Gutmark, E. (2015). Investigation of slurry concentration effects on solid particle erosion rate for an impinging jet. *Wear*, 342–343, 33–43. <https://doi.org/10.1016/j.wear.2015.08.003>
- Gandhi, B. K., Singh, S. N., & Seshadri, V. (1999). Study of the parametric dependence of erosion wear for the parallel flow of solid-liquid mixtures. *Tribology International*. [https://doi.org/10.1016/S0301-679X\(99\)00047-X](https://doi.org/10.1016/S0301-679X(99)00047-X)
- Grobler, P. E., & Mostert, R. J. (1990). Experience in the laboratory and commercial development of abrasion-corrosion resistant steels for the mining industry. *Wear*. [https://doi.org/10.1016/0043-1648\(90\)90035-9](https://doi.org/10.1016/0043-1648(90)90035-9)
- Grossmann, S., Lohse, D., & Sun, C. (2014). Velocity profiles in strongly turbulent Taylor-Couette flow. *Physics of Fluids*, 26(2), 1–30. <https://doi.org/10.1063/1.4865818>
- Grossmann, S., Lohse, D., & Sun, C. (2016). High-Reynolds Number Taylor-Couette Turbulence. *Annual Review of Fluid Mechanics*, 48(1), 53–80. <https://doi.org/10.1146/annurev-fluid-122414-034353>
- Hadavi, V., Moreno, C. E., & Papini, M. (2016). Numerical and experimental analysis of particle fracture during solid particle erosion, Part II: Effect of incident angle, velocity and abrasive size. *Wear*, 356–357, 146–157. <https://doi.org/10.1016/j.wear.2016.03.009>
- Hao, G., Dong, X., Du, M., Li, Z., & Dou, Z. (2019). A comparative study of ductile and brittle materials due to single angular particle impact. *Wear*, 428–429, 258–271. <https://doi.org/10.1016/j.wear.2019.03.016>
- Huang, C., Chiovelli, S., Mineev, P., Luo, J., & Nandakumar, K. (2008). A comprehensive phenomenological model for erosion of materials in jet flow. *Powder Technology*, 187(3), 273–279. <https://doi.org/10.1016/j.powtec.2008.03.003>

- Humphrey, J. A. C. (1990). Fundamentals of fluid motion in erosion by solid particle impact. *International Journal of Heat and Fluid Flow*, 11(3), 170–195. [https://doi.org/10.1016/0142-727X\(90\)90036-B](https://doi.org/10.1016/0142-727X(90)90036-B)
- Hussainova, I., Kubarsepp, J., & Pirso, J. (2001). Mechanical properties and features of erosion of cermets. *Wear*. [https://doi.org/10.1016/S0043-1648\(01\)00737-2](https://doi.org/10.1016/S0043-1648(01)00737-2)
- Hutchings, I. M. (1976). Solid particle erosion of metals: the removal of surface material by spherical projectiles. *Proceedings of the Royal Society of London. A. Mathematical and Physical Sciences*. <https://doi.org/10.1098/rspa.1976.0044>
- Hutchings, I. M. (1979). Energy absorbed by elastic waves during plastic impact. *Journal of Physics D: Applied Physics*. <https://doi.org/10.1088/0022-3727/12/11/010>
- Hutchings, I. M. (1981). A model for the erosion of metals by spherical particles at normal incidence. , 70(3, Aug. 15, 1981), 269–281. [https://doi.org/10.1016/0043-1648\(81\)90347-1](https://doi.org/10.1016/0043-1648(81)90347-1)
- Islam, M. A., Alam, T., Farhat, Z. N., Mohamed, A., & Alfantazi, A. (2015). Effect of microstructure on the erosion behavior of carbon steel. *Wear*, 332–333, 1080–1089. <https://doi.org/10.1016/j.wear.2014.12.004>
- Islam, M. A., & Farhat, Z. N. (2014). Effect of impact angle and velocity on erosion of API X42 pipeline steel under high abrasive feed rate. *Wear*, 311(1–2), 180–190. <https://doi.org/10.1016/j.wear.2014.01.005>
- Israel, R., & Rosner, D. E. (1983). Use of a generalized stokes number to determine the aerodynamic capture efficiency of non-stokesian particles from a compressible gas flow. *Aerosol Science and Technology*, 2(1), 45–51. <https://doi.org/10.1080/02786828308958612>
- Javaheri, V., Porter, D., & Kuokkala, V. T. (2018). Slurry erosion of steel – Review of tests, mechanisms and materials. *Wear*, 408–409(May), 248–273. <https://doi.org/10.1016/j.wear.2018.05.010>
- Jiménez, J. (1998). Turbulent velocity fluctuations need not be Gaussian. *Journal of Fluid Mechanics*, 376, 139–147. <https://doi.org/10.1017/S0022112098002432>
- Karson, M. (1968). *Handbook of Methods of Applied Statistics*. Volume I: Techniques of Computation Descriptive Methods, and Statistical Inference. Volume II: Planning of

- Surveys and Experiments. I. M. Chakravarti, R. G. Laha, and J. Roy, New York, John Wiley; 1967, \$9.00. *Journal of the American Statistical Association*, 63(323), 1047–1049. <https://doi.org/10.1080/01621459.1968.11009335>
- Kosa, E., & Göksenli, A. (2015). Effect of Impact Angle on Erosive Abrasive Wear of Ductile and Brittle Materials. *International Journal of Mechanical, Aerospace, Industrial, Mechatronic and Manufacturing Engineering*, 9(9), 1582–1586.
- Kuruvila, R., Kumaran, S. T., Khan, M. A., & Uthayakumar, M. (2018). A brief review on the erosion-corrosion behavior of engineering materials. *Corrosion Reviews*, 36(5), 435–447. <https://doi.org/10.1515/corrrev-2018-0022>
- Levy, A. V. (1981). The solid particle erosion behavior of steel as a function of microstructure. *Wear*. [https://doi.org/10.1016/0043-1648\(81\)90177-0](https://doi.org/10.1016/0043-1648(81)90177-0)
- Levy, A. V., & Chik, P. (1983). The effects of erodent composition and shape on the erosion of steel. *Wear*. [https://doi.org/10.1016/0043-1648\(83\)90240-5](https://doi.org/10.1016/0043-1648(83)90240-5)
- Liebhart, M., & Levy, A. (1991). The effect of erodent particle characteristics on the erosion of metals. *Wear*. [https://doi.org/10.1016/0043-1648\(91\)90263-T](https://doi.org/10.1016/0043-1648(91)90263-T)
- Lindgren, M., & Perolainen, J. (2014). Slurry pot investigation of the influence of erodent characteristics on the erosion resistance of austenitic and duplex stainless steel grades. *Wear*, 319(1–2), 38–48. <https://doi.org/10.1016/j.wear.2014.07.006>
- Lyashenko, I. A. (2019). Dynamic Model of Elastoplastic Normal Collision of a Spherical Particle with a Half-Space with Allowance for Adhesion Interaction in a Contact Zone. *Physics of the Solid State*, 61(2), 163–173. <https://doi.org/10.1134/S1063783419020161>
- Lyashenko, Iakov A., Willert, E., & Popov, V. L. (2018). Mechanics of collisions of solids: Influence of friction and adhesion. I. Review of experimental and theoretical works. *PNRPU Mechanics Bulletin*, (2), 44–61. <https://doi.org/10.15593/perm.mech/2018.2.05>
- Lynn, R. S., Wong, K. K., & Clark, H. M. I. (1991). On the particle size effect in slurry erosion. *Wear*. [https://doi.org/10.1016/0043-1648\(91\)90364-Z](https://doi.org/10.1016/0043-1648(91)90364-Z)
- Ma, L., Huang, C., Xie, Y., Jiang, J., Tufa, K. Y., Hui, R., & Liu, Z. S. (2015). Modeling of erodent particle trajectories in slurry flow. *Wear*, 334–335, 49–55. <https://doi.org/10.1016/j.wear.2015.04.013>

- Madsen, B. W. (1988). Measurement of erosion-corrosion synergism with a slurry wear test apparatus. *Wear*. [https://doi.org/10.1016/0043-1648\(88\)90095-6](https://doi.org/10.1016/0043-1648(88)90095-6)
- Mansouri, A., Shirazi, S. A., & McLaury, B. S. (2014). Experimental and numerical investigation of the effect of viscosity and particle size on the erosion damage caused by solid particles. American Society of Mechanical Engineers, Fluids Engineering Division (Publication) FEDSM. <https://doi.org/10.1115/FEDSM2014-21613>
- Messa, G. V., & Malavasi, S. (2017). The effect of sub-models and parameterizations in the simulation of abrasive jet impingement tests. *Wear*, 370–371, 59–72. <https://doi.org/10.1016/j.wear.2016.10.022>
- Messa, G. V., & Malavasi, S. (2018). A CFD-based method for slurry erosion prediction. *Wear*, 398–399(November 2017), 127–145. <https://doi.org/10.1016/j.wear.2017.11.025>
- Messa, G. V., Mandelli, S., & Malavasi, S. (2019). Hydro-abrasive erosion in Pelton turbine injectors: A numerical study. *Renewable Energy*, 130, 474–488. <https://doi.org/10.1016/j.renene.2018.06.064>
- Molina, N., Aguirre, J., & Walczak, M. (2019). Application of FFT analysis for the study of directionality of wear scars in exposure to slurry flow of varying velocity. *Wear*, 426–427(November 2018), 589–595. <https://doi.org/10.1016/j.wear.2019.01.013>
- More, S. R., Bhatt, D. V., & Menghani, J. V. (2017). Recent Research Status on Erosion Wear - An Overview. *Materials Today: Proceedings*, 4(2), 257–266. <https://doi.org/10.1016/j.matpr.2017.01.020>
- Morphological Image Analysis: Principles and Applications. (2000). *Sensor Review*, 20(3). <https://doi.org/10.1108/sr.2000.08720cae.001>
- Mouri, H., Takaoka, M., Hori, A., & Kawashima, Y. (2002). Probability density function of turbulent velocity fluctuations. *Physical Review E - Statistical Physics, Plasmas, Fluids, and Related Interdisciplinary Topics*, 65(5), 7. <https://doi.org/10.1103/PhysRevE.65.056304>
- Mouri, H., Takaoka, M., Hori, A., & Kawashima, Y. (2003). Probability density function of turbulent velocity fluctuations in a rough-wall boundary layer. *Physical Review E - Statistical Physics, Plasmas, Fluids, and Related Interdisciplinary Topics*, 68(3), 6. <https://doi.org/10.1103/PhysRevE.68.036311>

- Naim, M., & Bahadur, S. (1986). Effect of microstructure and mechanical properties on the erosion of 18 Ni (250) maraging steel. *Wear*. [https://doi.org/10.1016/0043-1648\(86\)90242-5](https://doi.org/10.1016/0043-1648(86)90242-5)
- Nandre, B. D., & Desale, G. R. (2018). Study the Effect of Impact Angle on Slurry Erosion Wear of Four Different Ductile Materials. *Materials Today: Proceedings*, 5(2), 7561–7570. <https://doi.org/10.1016/j.matpr.2017.11.428>
- Nguyen, Q. B., Nguyen, D. N., Murray, R., Ca, N. X., Lim, C. Y. H., Gupta, M., & Nguyen, X. C. (2019). The role of abrasive particle size on erosion characteristics of stainless steel. *Engineering Failure Analysis*, 97(December 2018), 844–853. <https://doi.org/10.1016/j.engfailanal.2019.01.020>
- Nguyen, Q. B., Nguyen, V. B., Lim, C. Y. H., Trinh, Q. T., Sankaranarayanan, S., Zhang, Y. W., & Gupta, M. (2014). Effect of impact angle and testing time on erosion of stainless steel at higher velocities. *Wear*, 321, 87–93. <https://doi.org/10.1016/j.wear.2014.10.010>
- Niu, S., Yang, J., Wang, S., & Chen, G. (2011). Improvement and parallel implementation of canny edge detection algorithm based on GPU. *Proceedings of International Conference on ASIC*, (6), 641–644. <https://doi.org/10.1109/ASICON.2011.6157287>
- Njobuenwu, D. O., & Fairweather, M. (2012). Modelling of pipe bend erosion by dilute particle suspensions. *Computers and Chemical Engineering*, 42, 235–247. <https://doi.org/10.1016/j.compchemeng.2012.02.006>
- O'Flynn, D. J., Bingley, M. S., Bradley, M. S. A., & Burnett, A. J. (2001). A model to predict the solid particle erosion rate of metals and its assessment using heat-treated steels. *Wear*. [https://doi.org/10.1016/S0043-1648\(00\)00554-8](https://doi.org/10.1016/S0043-1648(00)00554-8)
- Oka, Y. I., Matsumura, M., & Kawabata, T. (1993). Relationship between surface hardness and erosion damage caused by solid particle impact. *Wear*, 162–164, 688–695. [https://doi.org/10.1016/0043-1648\(93\)90067-V](https://doi.org/10.1016/0043-1648(93)90067-V)
- Oka, Y. I., Okamura, K., & Yoshida, T. (2005). Practical estimation of erosion damage caused by solid particle impact: Part 1: Effects of impact parameters on a predictive equation. *Wear*, 259(1–6), 95–101. <https://doi.org/10.1016/j.wear.2005.01.039>

- Oka, Y. I., & Yoshida, T. (2005). Practical estimation of erosion damage caused by solid particle impact: Part 2: Mechanical properties of materials directly associated with erosion damage. *Wear*, 259(1–6), 102–109. <https://doi.org/10.1016/j.wear.2005.01.040>
- Okonkwo, P. C., Mohamed, A. M. A., & Ahmed, E. (2015). Influence of particle velocities and impact angles on the erosion mechanisms of AISI 1018 steel. *Advanced Materials Letters*. <https://doi.org/10.5185/amlett.2015.5645>
- Omar, Y. M., Maragliano, C., Lai, C. Y., Iacono, F. Lo, Bologna, N., Shah, T., ... Chiesa, M. (2015). Holistic characterization of carbon nanotube membrane for capacitive deionization electrodes application. *Materials Research Society Symposium Proceedings*, (1752), 125–130. <https://doi.org/10.1557/opl.2015.253>
- Osman, O. S., Selway, J. L., Harikumar, P. E., Stocker, C. J., Wargent, E. T., Cawthorne, M. A., ... Langlands, K. (2013). A novel method to assess collagen architecture in skin. *BMC Bioinformatics*, 14(1), 1. <https://doi.org/10.1186/1471-2105-14-260>
- Pabst, W., & Gregorová, E. (2013). Elastic properties of silica polymorphs-a review. *Ceramics - Silikaty*, 57(3), 167–184.
- Parsi, M., Najmi, K., Najafifard, F., Hassani, S., McLaury, B. S., & Shirazi, S. A. (2014). A comprehensive review of solid particle erosion modeling for oil and gas wells and pipelines applications. *Journal of Natural Gas Science and Engineering*, 21, 850–873. <https://doi.org/10.1016/j.jngse.2014.10.001>
- Peng, P., & Wang, J. (2019). FECNN: A promising model for wear particle recognition. *Wear*, 432–433(July), 202968. <https://doi.org/10.1016/j.wear.2019.202968>
- Pereira, G. C., de Souza, F. J., & de Moro Martins, D. A. (2014). Numerical prediction of the erosion due to particles in elbows. *Powder Technology*, 261, 105–117. <https://doi.org/10.1016/j.powtec.2014.04.033>
- Raadnui, S. (2005). Wear particle analysis - Utilization of quantitative computer image analysis: A review. *Tribology International*, 38(10), 871–878. <https://doi.org/10.1016/j.triboint.2005.03.013>
- Ranjbar, M., Ghasemi, H. M., & Abedini, M. (2015). Effect of Impact Angle on the Erosion–Corrosion Behavior of AISI 420 Stainless Steel in 3.5 wt.% NaCl Solution. *Journal of Tribology*, 137(3), 031604. <https://doi.org/10.1115/1.4029939>

- Rohatgi, P. K., Tabandeh-Khorshid, M., Omrani, E., Lovell, M. R., & Menezes, P. L. (2013). Tribology for Scientists and Engineers. In *Tribology for Scientists and Engineers: From Basics to Advanced Concepts*. <https://doi.org/10.1007/978-1-4614-1945-7>
- Rosner, B. (1983). Percentage points for a generalized esd many-outlier procedure. *Technometrics*, 25(2), 165–172. <https://doi.org/10.1080/00401706.1983.10487848>
- Rueden, C. T., Schindelin, J., Hiner, M. C., DeZonia, B. E., Walter, A. E., Arena, E. T., & Eliceiri, K. W. (2017). ImageJ2: ImageJ for the next generation of scientific image data. *BMC Bioinformatics*, 18(1), 529. <https://doi.org/10.1186/s12859-017-1934-z>
- S. M Hsu, M. C. S. and A. W. R. (1997). Wear prediction for metals. *Tribology International*, 30(5), 377–383.
- Schober, P., & Schwarte, L. A. (2018). Correlation coefficients: Appropriate use and interpretation. *Anesthesia and Analgesia*, 126(5), 1763–1768. <https://doi.org/10.1213/ANE.0000000000002864>
- Shang, S., Yang, F., Cheng, X., Frank Walboomers, X., & Jansen, J. A. (2010). The effect of electrospun fibre alignment on the behaviour of rat periodontal ligament cells. *European Cells and Materials*, 19, 180–192. <https://doi.org/10.22203/eCM.v019a18>
- Sheldon, G. L. (1977). Effects of surface hardness and other material properties on erosive wear of metals by solid particles. *Journal of Engineering Materials and Technology, Transactions of the ASME*. <https://doi.org/10.1115/1.3443422>
- Shitole, P. P., Gawande, S. H., Desale, G. R., & Nandre, B. D. (2015). Effect of Impacting Particle Kinetic Energy on Slurry Erosion Wear. *Journal of Bio- and Tribo-Corrosion*, 1(4), 1–9. <https://doi.org/10.1007/s40735-015-0028-6>
- Sinha, S. L., Dewangan, S. K., & Sharma, A. (2017). A review on particulate slurry erosive wear of industrial materials: In context with pipeline transportation of mineral-slurry. *Particulate Science and Technology*, 35(1), 103–118. <https://doi.org/10.1080/02726351.2015.1131792>
- Stephens, M. A. (1974). EDF statistics for goodness of fit and some comparisons. *Journal of the American Statistical Association*, 69(347), 730–737. <https://doi.org/10.1080/01621459.1974.10480196>

- Suzuki, S., & be, K. A. (1985). Topological structural analysis of digitized binary images by border following. *Computer Vision, Graphics and Image Processing*, 30(1), 32–46. [https://doi.org/10.1016/0734-189X\(85\)90016-7](https://doi.org/10.1016/0734-189X(85)90016-7)
- Telfer, C. G., Stack, M. M., & Jana, B. D. (2012). Particle concentration and size effects on the erosion-corrosion of pure metals in aqueous slurries. *Tribology International*. <https://doi.org/10.1016/j.triboint.2012.04.010>
- Teng, H., Liu, N., Lu, X., & Khomami, B. (2015). Direct numerical simulation of Taylor-Couette flow subjected to a radial temperature gradient. *Physics of Fluids*, 27(12). <https://doi.org/10.1063/1.4935700>
- Thakare, M. R., Wharton, J. A., Wood, R. J. K., & Menger, C. (2012). Effect of abrasive particle size and the influence of microstructure on the wear mechanisms in wear-resistant materials. *Wear*. <https://doi.org/10.1016/j.wear.2011.11.008>
- Tressia, G., Penagos, J. J., & Sinatora, A. (2017). Effect of abrasive particle size on slurry abrasion resistance of austenitic and martensitic steels. *Wear*. <https://doi.org/10.1016/j.wear.2017.01.073>
- Truscott, G. F. (1972). A literature survey on abrasive wear in hydraulic machinery. *Wear*. [https://doi.org/10.1016/0043-1648\(72\)90285-2](https://doi.org/10.1016/0043-1648(72)90285-2)
- Tsai, W., Humphrey, J. A. C., Cornet, I., & Levy, A. V. (1981). Experimental measurement of accelerated erosion in a slurry pot tester. *Wear*. [https://doi.org/10.1016/0043-1648\(81\)90178-2](https://doi.org/10.1016/0043-1648(81)90178-2)
- Uzi, A., & Levy, A. (2018). Energy absorption by the particle and the surface during impact. *Wear*, 404–405(March), 92–110. <https://doi.org/10.1016/j.wear.2018.03.007>
- Uzi, A., & Levy, A. (2019). On the relationship between erosion, energy dissipation and particle size. *Wear*, 428–429(April), 404–416. <https://doi.org/10.1016/j.wear.2019.04.006>
- Valtonen, K., Ojala, N., Haiko, O., & Kuokkala, V. T. (2019). Comparison of various high-stress wear conditions and wear performance of martensitic steels. *Wear*, 426–427(December 2018), 3–13. <https://doi.org/10.1016/j.wear.2018.12.006>
- Walker, C. I., & Hambe, M. (2015). Influence of particle shape on slurry wear of white iron. *Wear*. <https://doi.org/10.1016/j.wear.2014.12.029>

- Walley & Field. (1987). The erosion and deformation of polyethylene by solid-particle impact. *Philosophical Transactions of the Royal Society of London. Series A, Mathematical and Physical Sciences*. <https://doi.org/10.1098/rsta.1987.0016>
- Wang, Huakun, Yu, Y., Yu, J., Xu, W., Li, X., & Yu, S. (2019). Numerical simulation of the erosion of pipe bends considering fluid-induced stress and surface scar evolution. *Wear*, 440–441(September), 203043. <https://doi.org/10.1016/j.wear.2019.203043>
- Wang, Hui, Yin, X., Hao, H., Chen, W., & Yu, B. (2020). The correlation of theoretical contact models for normal elastic-plastic impacts. *International Journal of Solids and Structures*, 182–183, 15–33. <https://doi.org/10.1016/j.ijsolstr.2019.07.018>
- Wang, S., Wu, T. H., Shao, T., & Peng, Z. X. (2019). Integrated model of BP neural network and CNN algorithm for automatic wear debris classification. *Wear*, 426–427(December 2018), 1761–1770. <https://doi.org/10.1016/j.wear.2018.12.087>
- Wang, Y. F., & Yang, Z. G. (2008). Finite element model of erosive wear on ductile and brittle materials. *Wear*, 265(5–6), 871–878. <https://doi.org/10.1016/j.wear.2008.01.014>
- Wilczek, M., Daitche, A., & Friedrich, R. (2011). Theory for the single-point velocity statistics of fully developed turbulence. *Epl*, 93(3), 1–6. <https://doi.org/10.1209/0295-5075/93/34003>
- Wilczek, Michael, Vlaykov, D. G., & Lalescu, C. C. (2017). Emergence of non-gaussianity in turbulence. *Springer Proceedings in Physics*, 196, 3–9. https://doi.org/10.1007/978-3-319-57934-4_1
- Willert, E. (2019). Energy loss and wear in spherical oblique elastic impacts. *Facta Universitatis, Series: Mechanical Engineering*, 17(1), 75–85. <https://doi.org/10.22190/FUME190115006W>
- Wood, E. J. (1990). Applying Fourier and Associated Transforms to Pattern Characterization in Textiles. *Textile Research Journal*, 60(4), 212–220. <https://doi.org/10.1177/004051759006000404>
- Xie, Y., Clark, H. M. I., & Hawthorne, H. M. (1999). Modelling slurry particle dynamics in the Coriolis erosion tester. *Wear*, 225–229(I), 405–416. [https://doi.org/10.1016/S0043-1648\(99\)00016-2](https://doi.org/10.1016/S0043-1648(99)00016-2)

- Xu, B. (1996). Identifying Fabric Structures with Fast Fourier Transform Techniques. *Textile Research Journal*, 66(8), 496–506. <https://doi.org/10.1177/004051759606600803>
- Yabuki, A., Matsuwaki, K., & Matsumura, M. (1999). Critical impact velocity in the solid particles impact erosion of metallic materials. *Wear*. [https://doi.org/10.1016/S0043-1648\(99\)00170-2](https://doi.org/10.1016/S0043-1648(99)00170-2)
- Zhang, Y., Reuterfors, E. P., McLaury, B. S., Shirazi, S. A., & Rybicki, E. F. (2007). Comparison of computed and measured particle velocities and erosion in water and air flows. *Wear*, 263(1-6 SPEC. ISS.), 330–338. <https://doi.org/10.1016/j.wear.2006.12.048>
- Zheng, S., Luo, M., Xu, K., Li, X., Bie, Q., Liu, Y., ... Liu, Z. (2019). Case study: Erosion of an axial flow regulating valve in a solid-gas pipe flow. *Wear*, 434–435(November 2018), 202952. <https://doi.org/10.1016/j.wear.2019.202952>

APPENDIX

APPENDIX A: SAMPLE MACHINING

The parameters recommended for machining copper are shown in Table 11:

Table 11. Machining parameters for Cu-ETP recommended by ASM/DKI.

Operation	Parameters	Cutting tool				
		HSS		Carbide		
		min	max	min	Max	
Turning	Cutting speed (rpm)	488	976	1952	3225	
	Cutting feed (mm/rev)	2	8	2	8	
	Expected chip thickness, at given cutting speed (mm)	0.63	0.10	0.80	0.10	
Drilling	Cutting speed (rpm)	488	976	1952	3225	
	Cutting feed (mm/rev) Drill diameter (mm)	5 - 8	0.16	0.25	0.12	0.18
		8 - 12	0.25	0.32	0.18	0.23
Reaming	Cutting speed (rpm)	170	573	170	573	
	Cutting feed (mm/rev)	0.23	0.61	0.23	0.61	

APPENDIX B: PARTICLE MORPHOLOGY

The shape and size of the erodent particles as seen under scanning electron microscope (SEM) are shown in Fig. 28 for the different particle size ranges.

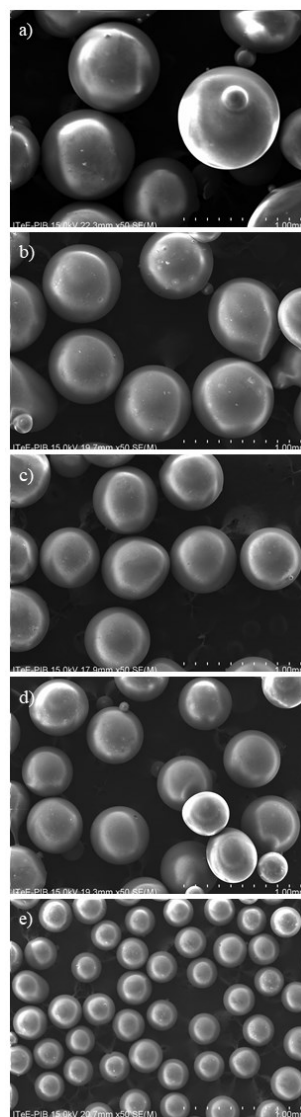


Figure 28. Representative SEM appearance of the erodent. Glass beads sieved by the mesh sizes: a) 20-25, b) 25-30, c) 30-35, d) 34-40, and e) 50-60.

APPENDIX C: CORROSION BY-PRODUCTS

Figure S2 shows the surface of copper after exposure equivalent to that described in the experimental procedure, but without the erodent. This experiment was conducted to verify the presence of corrosion by products. In Figure 29a, after 1 h of exposure, there was no presence of uniform corrosion in the Cu-ETP surface. The white spots correspond to minerals present in the distilled water (calcium, magnesium) as verified by EDX. Only in some places were a few local oxide layers were found on the surface (example in Fig. 29b), but it was a local trend rather than general.

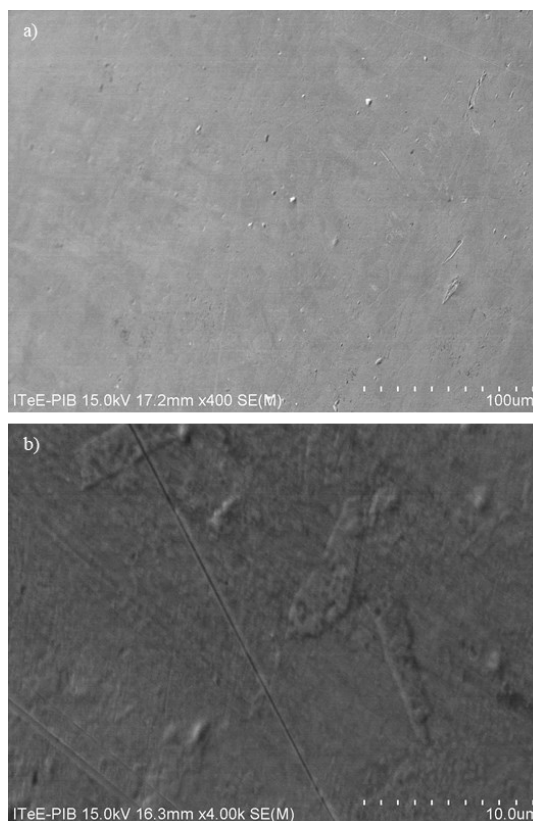


Figure 29. Example of SEM surface conditions after 1 h of exposure in distilled water. Nominal speed at the shaft surface 10 m/s. General appearance at magnification $\times 400$ (a) and example of local appearance at magnification $\times 4,000$ (b).